An Eigendecomposition-based and Mesh-sensitivity Reduced Constitutive Model for Nonlinear Analysis of Concrete Structures under Non-proportional Cyclic Loading

Terry Y.P. Yuen[a*], Tzu-Han Wen[a], Chung-Chan Hung[b], Hexin Zhang[c], Phu Anh Huy Pham[b], Yu Deng[d]

[a] Department of Civil Engineering, National Yang Ming Chiao Tung University, Hsinchu 30010, Taiwan (R.O.C.)

[b] Department of Civil Engineering, National Cheng Kung University, Tainan City 701, Taiwan (R.O.C.)

[c] School of Engineering and the Built Environment, Edinburgh Napier University, Edinburgh, Scotland, United Kingdom

[d] School of Civil Engineering and Architecture, Guangxi University of Science and Technology, Liuzhou, China, 545006

ABSTRACT

Emerging 3D printed concrete techniques has raised numerous possibilities in contemporary architectural creations that are often beyond the scope of prevailing structural design standards. Rigorous, three-dimensional, and nonlinear finite element analysis (NLFEA) with appropriate constitutive modelling of materials would be inevitable when analysing complex structures. However, many existing concrete models could hardly handle those structures' complicated behaviour, including crack-induced anisotropy, changeable stress transfer mechanisms, shear-slip and re-contact, mesh-size sensitivity, etc. Hence, this paper has developed a novel and experimentally validated constitutive model to tackle the above issues. The novel features include (1) highly robust total-strain formulation, (2) cyclic normal and tangential stress-strain responses, (3) a novel algorithm for uniquely fixing the 3D crack plane coordinate, (4) the equivalent strain transformation for modelling the axial-lateral strain interaction, (5) shear-slip and re-contact behaviour of cracks, and (6) mesh-size sensitivity mitigation. The proposed model was

* Corresponding author. E-mail address: terryyyp@nctu.edu.tw

implemented into ABAQUS's user-subroutine and applied to simulate a full-scale column test with specimen height = 5 m. The tested column, subjected to a constant vertical load and a cyclic load in the horizontal direction, failed in shear. The simulation can capture the damage evolutions and hysteresis response of the tested column. Hence, the proposed modelling framework could serve as a basis for analysing and designing concrete structures with unconventional shapes under non-proportional loading.

Keywords:

Constitutive model; anisotropy; shear-slip and re-contact; mesh-sensitivity reduced; non-proportional loading; concrete; finite element

1. Introduction

Concrete, a type of quasi-brittle material, remains one of the most consumed materials only next to water [1]. The popular design and analysis methods [2,3] for concrete structures are simplified strength-based and empirical-based methods applied to typical and regular structural members. However, the emerging 3D printed concrete techniques [4] have raised unbounded possibilities for constructing concrete structures of unconventional and complex shapes. However, many prevailing design standards do not allow the conventional or elastic methods to be used for complexly shaped structures [5,6] due to the possible severe stress and strain localisation. Three-dimensional nonlinear finite element analysis (3D-NLFEA) could be the only feasible option for designing the next generation of concrete structures that might feature non-conventional shapes and complicated loading conditions.

The essential ingredient in NLFEA is undoubtedly the constitutive models of the materials. Anisotropic mechanical responses of quasi-brittle materials could result from discontinuities in the strain field. But such anisotropicity is ignored by classical plasticity or coupled damage-plasticity models that assume isotropic hardening/softening rules [7–12]. Although those models may give reliable simulations under proportional loading conditions, they have remained the most popular models due to their simplicity in numerical implementations and parameter calibrations. Some advanced anisotropic damage models [13–17] can adequately capture the anisotropic inelastic responses. However, many parameters defining the evolution laws of the damage, yield, and flow rule often require excessive calibration work. Genetic algorithms were even proposed for estimating the many unknown parameters of the anisotropic damage model [18].

On the other hand, micro-plane or micromechanics models [19–21] process a manageable number of parameters. However, the procedure of mapping the micro-plane stress to the macroscopic stress of a representative volume element involves the evaluation of a 21-point numerical integration to attain sufficient accuracy [22]. A 37-point numerical integration scheme is even needed for significant

softening behaviour [23]. The high computational demand of micro-plane models may have restricted the applications to material design [24] and limited nonlinear structural analysis of small size members such as beams under impact [25] over an extremely short period of only milliseconds, and fracture behaviour of notched beams [26]. For practical analysis of the nonlinear behaviour of realistic large-scale reinforced concrete structures under extreme events with a lengthy time scale such as earthquakes and hurricanes, models with higher computational efficiency and quick parameter calibrations based on standard material tests are desired.

The other side of the concrete modelling spectrum features the phenomenological approach. The modified compression field theory (MCFT) [27,28] and fixed angle softened truss (FAST) or softened membrane model (SMM) [29,30] are the two widely adopted models for the nonlinear structural analysis of planar RC elements. Those models repeatedly demonstrated to show good agreement with experimental results and computational efficiency [31–34]. Uniaxial stress-total strain relationships with or without shear stress transfer were prescribed on the assumed crack planes by those models. Based on the assumption of orthogonal cracks [27,29,35], the stresses on the crack planes can be readily transformed to the global coordinates using Mohr's circle. Due to the adoption of the total strain formulations, implementation of those models in displacement-based finite element codes would suffer little or no convergence issues when the material softening occurs. However, the MCFT and SMM/FAST were formulated for 2D stress elements only and necessitate the proportional loading condition [36] due to the assumption of coincidence of principal stress and principal strain directions, which is valid only for isotropic elastic materials. This assumption becomes invalid if shear stress occurs on the crack planes due to aggregate interlocking. Even for flexure-controlled RC members under incremental reversed cyclic loading in the same directions, the shear effects would be increasingly significant with the crack severity in the plastic hinges [5]. To generalise the formulations to 3D cases, eigendecomposition of the stress and strain tensors have substituted the traditional Mohr' circle analysis [37]. Another successful

attempt on the 3D generalisation was done by Mullapudi and Ayoub [38], who employed the 3D Timosheko beam element with the softened membrane model to simulate columns subjected to combined axial, shear, flexure, and torsion loading. Their model formulations comply with the equilibrium and compatibility requirements in the 3D space. Yet, the uniqueness of the orthogonal crack plane coordinates needs to be addressed for general 3D solid-element implementations. Furthermore, the deviation of the principal stress and principal strain directions and the shear stress on the crack planes must be accounted for if non-proportional loading condition applies.

Moreover, the employment of continuum finite elements with conventional constitutive models for the simulation of material damage or softening behaviour could be mesh-sensitive [39]. Nonlinear responses time history analysis [5,40] is often needed to design irregular concrete and brittle structures under earthquake excitations. This type of analysis would involve the modelling of softening and extensive damage behaviour, and therefore, the mesh-sensitive issues should be resolved.

Given the above issues, this paper presents a new, robust, and computationally-efficient constitutive model for concrete structures. The model is formulated based on eigendecomposition and the rigorous cyclic stress-strain behaviour prescribed on the fixed crack planes and was successfully implemented in ABAQUS using the user-subroutine. The modelling parameters can be readily determined from or correlated with the data of standard material tests. The model could capture a wide range of inelastic behaviour of concrete under non-proportional loading. Lastly, the model was adopted to simulate a real-scale RC column test, and a good agreement between the experimental and simulated behaviour could be observed. Moreover, structures made of quasi-brittle, fibre-reinforced cementitious composites [41] and 3D printed concrete exhibiting heterogeneous stiffness properties [4] can also be simulated by the proposed model using appropriate constitutive laws. Hence, the modelling framework presented in this paper could serve as a basis for analysing and designing the non-conventionally shaped concrete structures subject to non-proportional loading.

2. Model development

2.1 Overview

This section presents the overall framework, principles, and general behaviour of the constitutive model development. The proposed model utilised the phenomenological stress-total strain relationships on the cracked planes supported by well-established experimental results. The crack planes are assumed to be orthogonal to each other once formed. A crack plane except for the third crack plane occurs when the principal stresses exceed the prescribed crack strengths. Since the second crack plane cannot be uniquely defined following the formation of the first crack, a novel searching algorithm was developed to fix the crack-plane coordinate. Meanwhile, the third potential crack direction can be uniquely determined after the formation of the second crack due to the orthogonality constraint.

At a given time, the strain increments and stored internal variables in the global coordinate are passed to an element's material point or integration point. The total strains are first calculated and transformed to the crack coordinate. Then, the equivalent uniaxial strains, which are used to calculate the effective normal stresses on the crack planes, are obtained by subtracting the strains due to Poisson's effect from the total strains. The shear retention relationship calculates the shear stress on crack planes. Lastly, the stresses in the crack coordinate are mapped back to the global coordinate using the contravariant tension transformation, and the internal variables at that material point are updated. A regularisation method for modifying the model parameters based on the element characteristic length is proposed to mitigate the mesh-size sensitivity issues when material softening occurs.

2.2 Constitutive modelling of cracked concrete

The detailed mathematical formulations of the constitutive are presented in this section. The eigendecomposition and the crack plane formation criteria based on the principal stresses are first

discussed in section 2.2.1. Then, the stress-strain models along the normal and the tangential directions of the crack planes are presented in section 2.2.2. The transformation of the equivalent uniaxial strains from the total axial strains with the modified Hsu/Zhu ratio is provided in section 2.2.2.

2.2.1 Eigen-decomposition and crack plane directions

The principal stresses σ_j or strains ε_j can be obtained by solving the eigenvalue problems for the stress tensor $\tilde{\boldsymbol{\sigma}}$ and the strain tensor $\tilde{\boldsymbol{\varepsilon}}$ in the Cartesian coordinate system.

$$\left(\tilde{\boldsymbol{\sigma}} - \sigma_j \mathbf{I}\right) \cdot \mathbf{V_j} = \mathbf{0}; \quad \left(\tilde{\boldsymbol{\varepsilon}} - \bar{\varepsilon}_j \mathbf{I}\right) \cdot \breve{\mathbf{V}}_{\boldsymbol{j}} = \mathbf{0} \tag{1}$$

where $\mathbf{I}$ is the identity tensor; $\mathbf{V_j}$ & $\breve{\mathbf{V}}_{\boldsymbol{j}}$ are the unit direction vectors of the corresponding principal stress σ_j and principal strain $\bar{\varepsilon}_j$ respectively. The order of the principal stresses/strains is taken as $\sigma_1 \geq \sigma_2 \geq \sigma_3$. The direction vectors form the orthonormal basis i.e. $\mathbf{V_i^T} \cdot \mathbf{V_j} = \delta_{ij}$, where δ_{ij} is Kronecker delta. The inverse of the directional vectors $\mathbf{V_j}$ and $\breve{\mathbf{V}}_{\boldsymbol{j}}$ are their transposes $\mathbf{V_j^T}$ and $\breve{\mathbf{V}}_{\boldsymbol{j}}^{\boldsymbol{T}}$ respectively. By using these inverse properties and Eq. (1), we have

$$\mathbf{V_i^T} \cdot \tilde{\boldsymbol{\sigma}} \cdot \mathbf{V_j} = \boldsymbol{\sigma}; \quad \breve{\mathbf{V}}_{\boldsymbol{i}}^{\boldsymbol{T}} \cdot \tilde{\boldsymbol{\varepsilon}} \cdot \breve{\mathbf{V}}_{\boldsymbol{j}} = \bar{\boldsymbol{\varepsilon}} \tag{2a}$$

$$\mathbf{V_j} \cdot \boldsymbol{\sigma} \cdot \mathbf{V_i^T} = \tilde{\boldsymbol{\sigma}}; \quad \breve{\mathbf{V}}_{\boldsymbol{j}} \cdot \bar{\boldsymbol{\varepsilon}} \cdot \mathbf{V_i^T} = \tilde{\boldsymbol{\varepsilon}} \tag{2b}$$

where $\boldsymbol{\sigma} = \sigma_j \delta_{ij}$ and $\bar{\boldsymbol{\varepsilon}} = \bar{\varepsilon}_j \delta_{ij}$ are the stress and total strain tensors rotated to the principal directions with zero off-diagonal elements (i.e. shear components = 0). The above transformation is also known as contravariant tensor transformation. For isotropic elastic materials, the principal stress and principal strain directions coincide i.e. $\mathbf{V_j^T} \cdot \breve{\mathbf{V}}_{\boldsymbol{j}} = 1$. Yet, when a material deforms inelastically, the principal stress and strain directions, in general, do not coincide i.e. $\mathbf{V_j^T} \cdot \breve{\mathbf{V}}_{\boldsymbol{j}} \neq 1$. The causes of the non-coaxiality include the coupling of deviatoric and volumetric strains, plasticity/damage-induced anisotropy, and

plastic-strain development. The non-associate flow rule makes the strain tensor does not commute with the stress tensor i.e. $\tilde{\boldsymbol{\sigma}} \cdot \tilde{\boldsymbol{\varepsilon}} \neq \tilde{\boldsymbol{\varepsilon}} \cdot \tilde{\boldsymbol{\sigma}}$ that results in $\mathbf{V}_j^T \cdot \breve{\mathbf{V}}_j \neq 1$ [41], as the elastic-plastic stiffness matrix $\mathbf{K}_{ep}$ or the compliance matrix $\mathbf{S}_{ep} = \mathbf{K}_{ep}^{-1}$ are no longer symmetric and isotropic in this situation [42]. The directional cosines $\cos \alpha_{ij}$ of the principal stress direction vectors in Cartesian coordinates with the basis $\boldsymbol{e}_j$ are given as

$$\cos \alpha_{ij} = \mathbf{V}_i^T \cdot \boldsymbol{e}_j \text{ in which } \sum_{j=1}^{n} \cos^2 \alpha_{ij} = 1 \tag{3}$$

It is noted that $2\alpha_{ij}$ is equal to the rotation angle of Mohr's circle representation for the stress/strain transformation.

Meanwhile, increasing concrete compression causes microscopic wing cracks, which are generally nucleated from the weak interfacial transition zone (ITZ) between the aggregates and cement pastes [43]. As the number and size of the wing cracks continue to grow, the interaction or coalescence of the cracks will occur and lead to system instability [44], i.e. compressive fracture. The crack direction resulting from the compressive fracture is influenced by the boundary restraints and confining pressure [45]. Under low lateral confinement, splitting cracks would occur and the crack opening is perpendicular to the compression direction, i.e. $\mathbf{V}_j^c = \mathbf{V}_3^{\perp}$. However, under high lateral confinement, shear cracks would occur with the propagation direction being deviated from the principal compression direction. As a low-confinement situation is assumed in this study, the splitting crack mode would occur under the compressive fracture. Such assumption is consistent with the compression field theory [27]. Furthermore, although little to no visible macroscopic cracks due to the wing-crack coalescence would be observed when concrete is compressed in the pre-peak regime [43], an increase of mortar cracking could be observed above 70% of the peak stress [46]. Strain localisation along the loading axis could occur around 80% of the peak stress [47]. Hence, it could be assumed that a preferred crack orientation could emerge under compression at $\sigma_3 = c_{\mathrm{ck}} f_c$ with $1.0 \geq c_{\mathrm{ck}} \geq 0.7$ and the corresponding crack

opening direction is $\mathbf{V}_j^c = \mathbf{V}_3^{\perp}$. Yet, the macrosopic splitting crack would not form until the peak compressive strength f_c is reached [43].

The first crack plane (preferred crack orientation) is assumed to occur at a specific angle α_c measured from the x-axis $\boldsymbol{e_x}$, when one of the following criteria is satisfied.

$$\alpha_c = \alpha_{11} + \pi/2 \qquad \text{if } \sigma_1 = f_t > 0 \tag{4a}$$

$$\alpha_c = \alpha_{31} \qquad \text{if } \sigma_3 = c_{ck}\xi f_c < 0 \tag{4b}$$

The normal directional vector of the j[th] crack plane is directly obtained from the eigenvectors as

$$\mathbf{V}_j^c = \mathbf{V_1} \qquad \text{if } \sigma_1 = f_t > 0 \tag{5a}$$

$$\mathbf{V}_j^c = \mathbf{V}_3^{\perp} \qquad \text{if } \sigma_3 = c_{ck}\xi f_c < 0 \tag{5b}$$

where ξ is the compressive strength modification factor, and its physical meaning will be introduced later. For 2D problems, the vector perpendicular to the principal compressive stress $\mathbf{V}_3^{\perp}$ shall satisfy $\mathbf{V}_i^T \cdot \mathbf{V}_3^{\perp} \equiv 0$ and therefore, it is simply equal to $\mathbf{V_1}$. But it becomes indeterministic for 3D problems unless another vector lying on the crack plane is found. Physically, cracks tend to open in the maximum tensile strain/stress direction $\breve{\mathbf{V}}_1$ or $\mathbf{V_1}$ and the principal direction $\breve{\mathbf{V}}_2$ or $\mathbf{V_2}$ of the immediate stress/strain shall lie on the crack plane. As a result, the norm of the crack plane also coincides with $\breve{\mathbf{V}}_1$ or $\mathbf{V_1}$. The crack direction cannot be resolved in axisymmetric problems where $\mathbf{V_1} = \mathbf{V_2}$, but they can be transformed into equivalent 2D problems.

2.2.2 Stress-strain relationship in the crack plane coordinates

Based on a series of panel shear tests, Vecchio & Collins (1986) [27] and Hsu & Mansour (2005) [48] developed constitutive laws for planar cracked concrete, which is represented by diagonal struts prescribed with uniaxial stress-strain relationships along ($\mathbf{V_3^c}$) and perpendicular ($\mathbf{V_1^c}$) to the crack plane as shown in **Fig. 1**. As discussed above, after the crack formation, the responses of the material become anisotropic and the principal stress and strain directions do not coincide. Therefore, shear stress can occur if the shear strain is induced on the concrete crack plane upon the subsequent loading. The rough cracked surface's tangential shear stiffness or friction would not vanish due to the aggregate interlocking or shear retention [27,42] when the crack opening is small.

When the loading direction is reversed, the second crack plane in the same and sufficiently small material element can be assumed to be perpendicular to the first crack plane [35,49]. Furthermore, the orthogonal crack planes can be fixed on $\mathbf{V_1^c}$ & $\mathbf{V_3^c}$ right after the crack initiation. To model the behaviour of such pair of diagonal struts, an improved stress-strain relationship based on Hsu & Mansour (2005) has been developed and is outlined below. The main modifications include (1) a new unloading curve that is based on the concept of plastic-strain and crack-strain decomposition from the compression envelope, (2) the minimum compressive strength that is used to prevent numerical instability, (3) the residual strength–dependent unilateral points for the stiffness recovery from tension to compression transition, (4) the introduction of shear stress-strain behaviour on the cracked planes, and (5) modified Poisson's effect under different stress states.

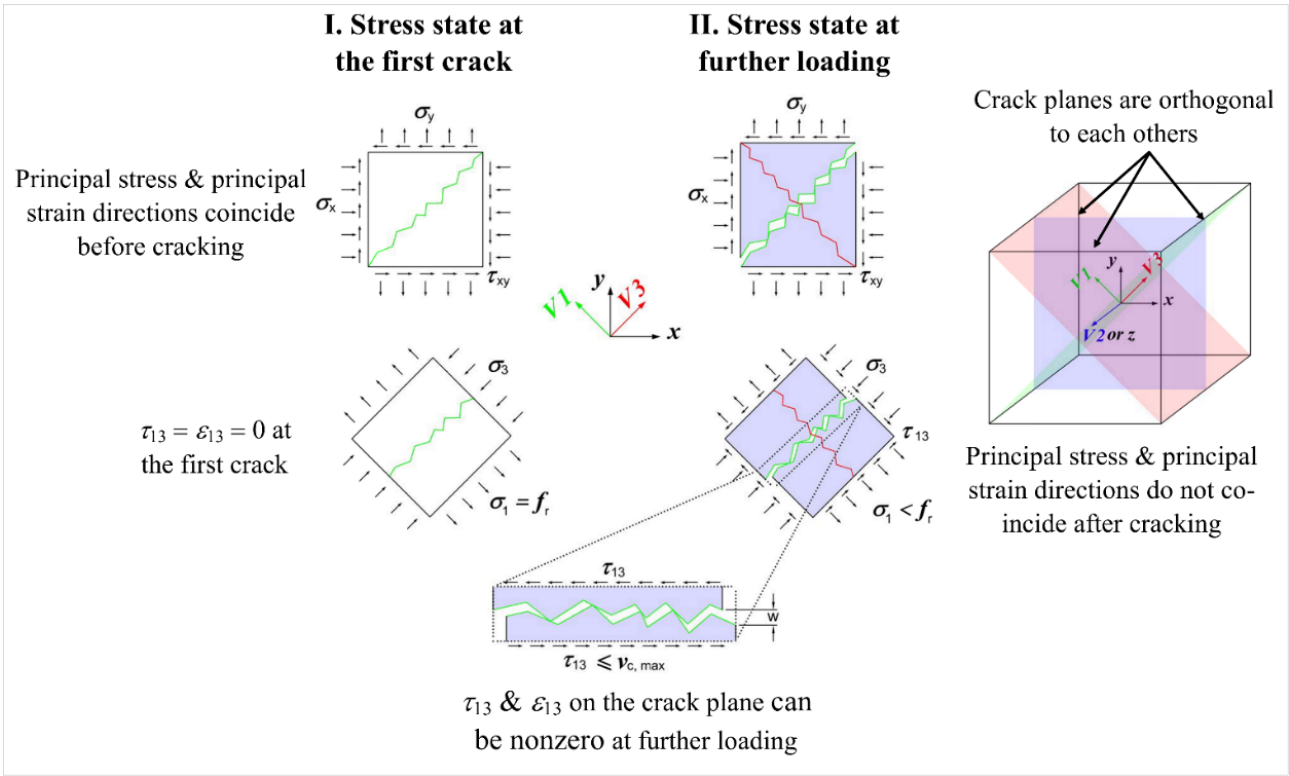

Fig. 1. Stress states at the first crack and upon further loading.

Uniaxial behaviour

If the concrete along the direction $\mathbf{V_3^c}$ is under compression, then the ascending and descending branches of the compression envelope of the stress σ_3 and the equivalent axial strain ε_3 curves are expressed by Eqs. (6a) & (6b) respectively.

$$\sigma_3 = (D\zeta f_c - f_{c4})\left[2\left(\frac{\varepsilon_3}{\zeta\varepsilon_o}\right) - \left(\frac{\varepsilon_3}{\zeta\varepsilon_o}\right)^2\right] + f_{c4} \qquad \text{if } \zeta\varepsilon_o \leq \varepsilon_3 \leq 0 \qquad (6a)$$

$$\sigma_3 = \max\left(D\zeta f_c\left[1 - \left(\frac{\varepsilon_3/(\zeta\varepsilon_o)-1}{a_c/\zeta-1}\right)^2\right], c_{min}\,\zeta f_c\right) \qquad \text{if } \zeta\varepsilon_o > \varepsilon_3 \qquad (6b)$$

The state-variables D and ζ, which control the softening of the compressive strength $f_c < 0.0$, are calculated by Eq. (7) and Eq. (8) respectively; f_{c4} is defined in **Fig. 2;** D depends on the maximum compressive strain $\varepsilon_c^{\mathrm{Max}}$ in the past loading history, while ζ is the multiplication of three strength

reduction factors $\zeta_1(f_c)$, and $\zeta_2(\varepsilon_1 \geq 0)$; a_c is a mesh-size dependent constant governing the decay rate of the compressive stress after the peak. The tensile strain $\varepsilon_1 \geq 0$ along the direction $\mathbf{V_1^c}$ which is perpendicular to $\mathbf{V_3^c}$. The second term of Eq. (6b) represents the minimum compressive strength and is used to prevent numerical instability. The factor c_{min} is set as 0.01 in this study.

$$D = 1 - \psi \frac{\varepsilon_c^{\text{Max}}}{\varepsilon_o} \leq 1.0 \qquad \varepsilon_c^{\text{Max}} < 0 \tag{7}$$

$$\zeta = \zeta_1(f_c) \cdot \zeta_2(\varepsilon_1 \geq 0) = \left(\frac{5.8}{\sqrt{f_c}} \leq 0.9\right) \cdot \left(\frac{1}{\sqrt{1+400\varepsilon_1}}\right) \tag{8}$$

where ψ is a parameter controlling the effect of cyclic damage on the compressive strength. If the concrete along the direction $\mathbf{V_1^c}$ is under tension, then the stress-strain envelope can be expressed by Eqs. (9a) and (9b) for the pre-peak and post-peak branches, respectively.

$$\sigma_1 = E_c \varepsilon_1 \qquad \text{if } \varepsilon_r \geq \varepsilon_1 \geq 0 \tag{9a}$$

$$\sigma_1 = \alpha_{CD} f_r \left(\frac{\varepsilon_r}{\varepsilon_1}\right)^{a_t} \qquad \text{if } \varepsilon_1 > \varepsilon_r \tag{9b}$$

where f_r is the peak tensile stress and $\varepsilon_r = f_r/E_c$ is the corresponding strain; a_t is a mesh-size dependent constant governing the decay rate of the post-peak tensile stress; α_{CD} is the ratio between the residual compressive strength f_{c2} (**Fig. 2**) and the peak compressive strength $\zeta_1 f_c$ as defined by Eq. (10).

$$\alpha_{CD} = f_{c2}/(\zeta_1 f_c) \leq 1.0 \tag{10}$$

Under cyclic compression, the stress initially follows the envelope curves given by Eqs. (6), which has a peak at C1 ($\zeta\varepsilon_o$, ζf_c). Upon load reversal, the material is unloaded from C2 (ε_{C2}, f_{c2}) to C3($b_{\text{C}}\varepsilon_{\text{C2}}$, 0.0) with a softened stiffness $E_{c23} = f_{c2}/\big(\varepsilon_{\text{C2}}(1 - b_{\text{C}})\big) \leq E_c$. If the material is reloaded in compression at C4 (ε_{C4}, f_{c4}), the stress-strain curve will point toward C5 ($(2(\varepsilon_{\text{C2}} - f_{c2}/E_c) + \varepsilon_{\text{C4}})/3$, $0.2f_{c2}$). After

C5, the stiffness increases, and the loading curve will pass through C6 ($0.98\varepsilon_{C2}$, $0.85f_{c2}$). Once the stress touches the envelop curve, the subsequent loading curve follows Eqs. (6).

Under cycle tension, the stress initially follows the tension envelope given by Eq. (9). If the material is loaded beyond the peak stress T1 (ε_r, f_r) and then unloaded at T2 (ε_{T2}, f_{T2}), the unloading curve will point toward T3 ($\varepsilon_{T2}/3$, $-0.2\alpha_{CD}f_r$) with a softened stiffness. The stiffness recovery can be observed for continuous compression of the material after passing T3, and the stress will pass through T4 (0.0, $(-1.5f_r + 0.8f_{T2}) \cdot \alpha_{CD}$) until touching the compressive envelop again.

For $b_C = 0.0$, the unloading curve is origin-oriented, which results in no plastic strain or pure cracking, while for $b_C = 1 - f_{c2}/E_c\varepsilon_{C2}$, the unloading stiffness is the same as the initial stiffness, i.e. $E_{c23} = E_c$, which results in no crack strain or pure plastic deformation. Hence, b_C is a parameter controlling the ratio between the plastic strain and the cracking strain [10]. The inelastic strain is accumulated in the compressive loading cycle from C2 to C2', and this is known as the ratcheting phenomenon that can cause low-cycle fatigue of materials [50].

Meanwhile, the factor α_{CD} for T3 and T4 as defined by Eq. (10) is used to eliminate the abnormal behaviour of the original model for the stress at the stiffness recovery (unilateral) point T4 from tension to compression. Without the damage factor α_{CD}, the stress at T4 unrealistically remains constant even if the compressive strength is exhausted completely. Meanwhile, the cyclic loading effect on the compressive strength degradation is reflected by the factor D as given by Eq. (7). The parameter ψ controls the decay rate and its influences on the cyclic behaviour are illustrated in **Fig. 3**.

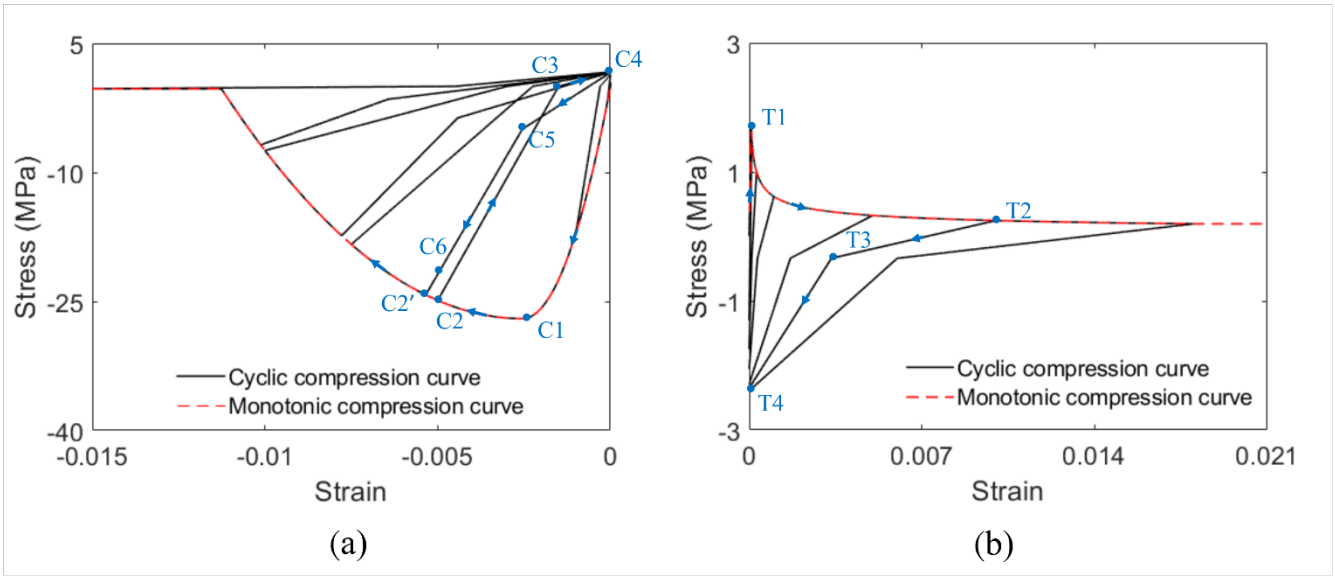

The strain at point C3, $b_C\varepsilon_{C2}$, is the plastic strain, which is assumed to be proportional to the total strain under compression. The proportional constant b_C shall be within the range given below.

$$0.0 \leq b_C \leq 1 - f_{c2}/(E_c\varepsilon_{C2}) \tag{11}$$

Shear behaviour

The shear stress on the crack plane is zero at the crack initiation, but the shear stiffness will not vanish due to the aggregate interlocking. Therefore, shear stress will be present on crack planes if the shear strain is induced during the subsequent loading [35]. Cyclic Softening Membrane Model (CSMM) [30] assumes that the principal stress directions $\mathbf{V_j}$ and the principal strains directions $\tilde{\mathbf{V}}_\mathbf{j}$ coincide and therefore the shear stress on the crack plane can be directly calculated by using the uniaxial stresses and strains on $\mathbf{V_1^c}$ & $\mathbf{V_3^c}$ with Eq. (12).

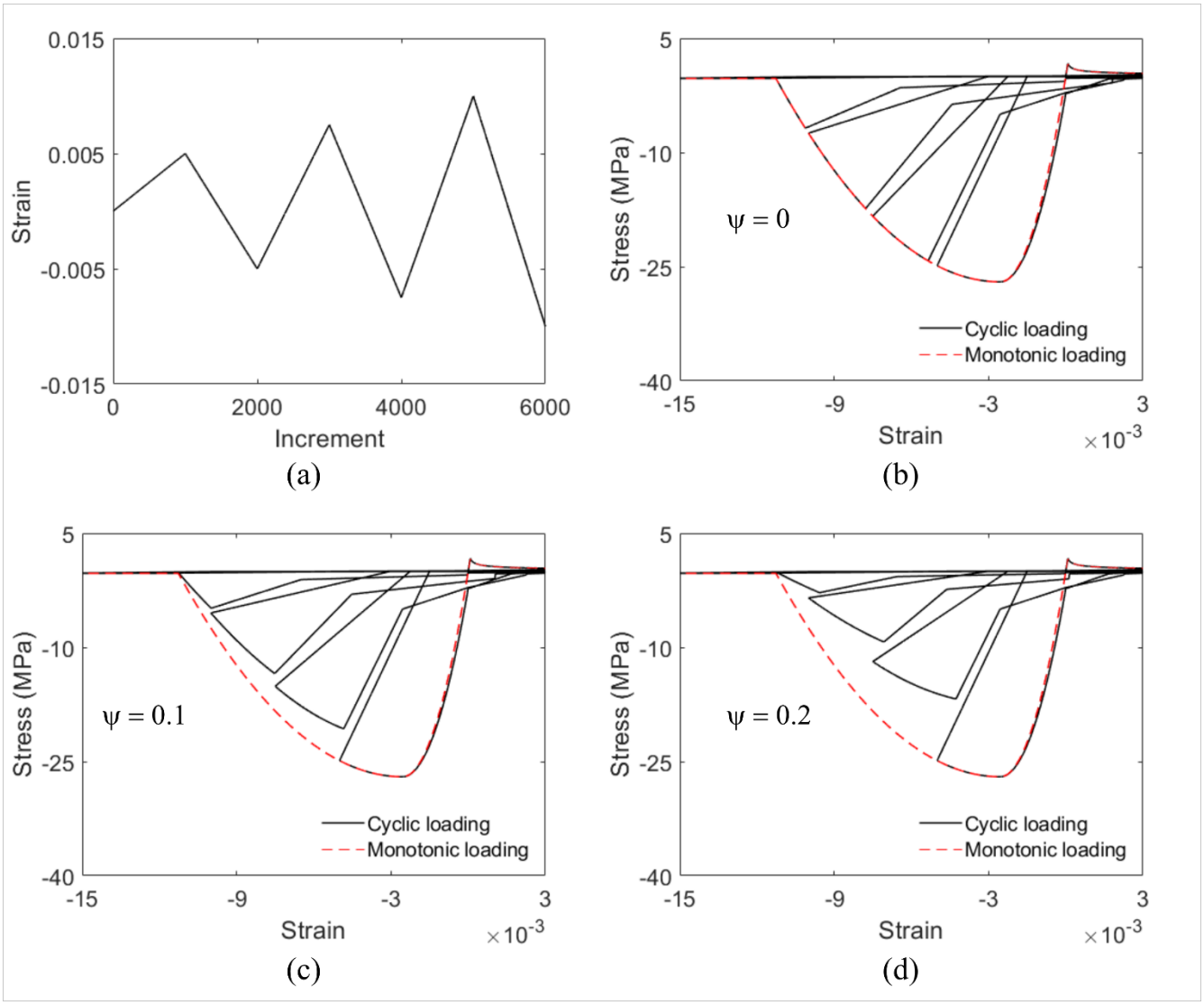

Fig. 3. Under a cyclic strain history (a), the strength degradation can be controlled by the parameter ψ. No degradation will occur for (b) $\psi = 0$, while various degrees of degradation will occur for none zero ψ, e.g. (c) $\psi = 0.1$ and (d) $\psi = 0.2$.

However, as discussed above, such an assumption is invalid and generally $\mathbf{V}_j^T \cdot \breve{\mathbf{V}}_j \neq 1$ for inelastic materials. The Modified Compression-Field Theory (MCFT) [27,28] also assumes $\mathbf{V}_j^T \cdot \breve{\mathbf{V}}_j = \mathbf{1}$, yet it allows the shear stress to exist on the crack planes. The maximum shear stress $\tau_{13,max}$ on a crack plane

$\mathbf{V_1^c}$ subjecting to shear in $\mathbf{V_3}$ is calculated by Eq. (13), which is based on the aggregate interlocking analysis by Walraven [51].

$$\tau_{13}^c = \frac{\sigma_1 - \sigma_3}{\varepsilon_1 - \varepsilon_3}\,\varepsilon_{13} \qquad \text{(CSMM)} \qquad (12)$$

$$\tau_{13}^c \le \tau_{c1,MCFT} = \hat{\tau}_{c1} + 1.64\langle -\sigma_1\rangle - 0.148\frac{\langle -\sigma_1\rangle^2}{\hat{v}_{c1}} \qquad \text{(MCFT)} \qquad (13)$$

where $\langle -\sigma_1\rangle = \sigma_1$ if $\sigma_1 < 0$ or $\langle -\sigma_1\rangle = 0$ if $\sigma_1 \ge 0$ and hence the last two terms of Eq. (13) account for the pressure-dependent friction.

Under the absence of normal compression on the crack plane $\mathbf{V_1^c}$ **,** the maximum shear stress $\tau_{c1,MCFT}$ is given by Eq. (14).

$$\hat{\tau}_{c1} = \frac{0.18\sqrt{-f_c}}{0.31 + 24 w_{1,max}/(D_a + 16)} \qquad \text{(in mm, N)} \qquad (14)$$

The maximum shear stress $\hat{v}_{c1}$ is a function of the maximum aggregate size D_a and the maximum crack width $w_{1,amx}$. In smeared crack models, w_1 can be estimated from the crack strain $\varepsilon_1^{cr} = \varepsilon_1 - f_r/E_c \ge 0$ and the element characteristic length crack l_e as

$$w_{1,max} = \varepsilon_{1,max}^{cr}\, l_e \qquad (15)$$

The element characteristic length crack l_e shall be less than the expected crack spacing L_{cs}, which depends on the reinforcement ratio and the material strengths, and it can be estimated by the Salem and Maekawa model [52] as

$$L_{cs} = 500\left(\frac{d}{19}\right)\left(\frac{1+f_r}{3}\right)\left(\frac{\rho_{e1}}{0.01}\right)^{-0.5}\left(\frac{f_y}{350}\right)^{-0.1}\left(\frac{f_c}{25}\right)^{-0.4} \qquad \text{(in mm, N)} \qquad (16)$$

in which ρ_{e1} is the effective reinforcement ratio in $\mathbf{V_1^c}$, d is the bar diameter and f_y is the yield strength of the reinforcement. For orthogonally reinforced concrete panels, ρ_{e1} can be calculated as

$$\rho_{e1} = \frac{(A_{sl}\boldsymbol{e_l} + A_{st}\boldsymbol{e_t})\cdot \mathbf{v_1}}{A_{RC}} = \rho_{el}\cos^2\alpha_{l1} + \rho_{et}\cos^2\alpha_{t1} \tag{17}$$

where A_{sl} & A_{st} are the area of reinforcement within the effective reinforced area A_{RC} with the corresponding effective reinforcement ratios ρ_{el} & ρ_{et} in the longitudinal ($\boldsymbol{e_l}$) and transverse ($\boldsymbol{e_t}$) directions respectively. $\cos\alpha_{l1} = \boldsymbol{e_l}\cdot\mathbf{V_1^c}$ & $\cos\alpha_{t1} = \boldsymbol{e_t}\cdot\mathbf{V_1^c}$.

The second and third terms of Eq. (13) depict the compressive stress-dependent frictional effect, where the coefficient of the linear term can be regarded as the coefficient of friction μ. In this study, the following generalised first-order friction model based on CEB-FIP (2010) [53] is used to calculate the maximum shear stress across the concrete-to-concrete interfacial crack

$$\tau_c = \hat{\tau}_c(w_i) + \mu\langle-\sigma_1\rangle \leq \tau_{c,max} \tag{18}$$

where $\hat{\tau}_c$ is given by Eq. (14) and μ depends on the roughness of the cracked surfaces; $\tau_{c,max}$ is the limit of τ_c. As per the recommendations by CEB-FIP (2010) [53] on concrete to concrete interfacial modelling,

$$\mu = \begin{cases} 0.5-0.7 & \text{Smooth interface} \\ 0.7-1.0 & \text{Rough interface} \\ 1.0-1.4 & \text{Very rough interface} \end{cases} \tag{19}$$

The equilibrium condition requires $\tau_{ij} = \tau_{ij}$. If cracks have formed on both $\mathbf{V_1^c}$ and $\mathbf{V_3^c}$, the maximum sustainable shear stress on these two crack planes would be limited by Eq. (18).

$$\tau'_{cij,max} = \min\left[\tau_{ci}\left(w_{i,max},\ \langle-\sigma_i\rangle\right), \tau_{cj}\left(w_{j,max},\ \langle-\sigma_j\rangle\right)\right] \tag{20}$$

The shear stiffness of cracked concrete can be independent of Young's modulus and Poisson's ratio. Furthermore, the maximum shear stress in Eq. (13) decreases with the crack opening w only. The most

common way to model this effect is to use a damage state-dependent shear retention factor $\beta_v \leq 1$ [54–56] to reduce the effective shear stiffness, i.e. $G_{eq} = \beta_v G_c$, where $G_c = E_c/\big(2(1+\nu_c)\big)$ is the initial shear modulus. The shear retention factor β_v could be as small as 0.01% after the crushing occurred [54]. This effect can also be modelled by reducing the maximum shear stress $v_{cij,max}$ with the damage factor $\alpha_{CD,ij}$ as defined in Eq. (11) of the relevant crack planes $\mathbf{V_i^c}$ and $\mathbf{V_j^c}$ such that the degradation rate of the maximum shear stress is consistent with that of the compressive strength, e.g.

$$\tau_{ij}^{c} = 2\beta_v G_c \varepsilon_{ij} \leq \tau'_{cij} \tag{21}$$

Meanwhile, the imperfect contact of the crack surfaces would lead to nonlinear elastic shear stress-strain behaviour. More complicated shear models such as the contact density model [35] can be used to model this behaviour. Based on the above model, the maximum attainable shear stress across a crack would degrade with the normal crack opening w but increase with the aggregate size D_a, which is an important feature of shear stress transfer due to aggregate interlocking [51]. The relations among the maximum attainable shear stress, the crack width, and aggregate size are illustrated in **Fig. 4**.

For a system with weak aggregate or high-strength cement paste, the aggregate strength would be comparable with the matrix strength. Then, the crack could cut through the aggregate, leaving a smooth crack surface. If the aggregate fracture is expected, the maximum attainable shear stress across a crack can be modified using the aggregate effectivity factor C_f according to CEB-FIP (2010) [53].

$$\tau'_{c,max} = \tau_{c,max}\, C_f \tag{22}$$

where C_f = 1.0 if the aggregate does not fracture upon cracking, C_f = 0.35 if most of the aggregate is expected to fracture upon cracking. In this study, the assumed cyclic behaviour, termed modified shear retention, is shown in **Fig. 4(c)**. The shear slip with $\tau = 0$ on the crack plane would occur during

unloading until the shear strain sign is reversed and the shear stress will pick up again. This behaviour is due to the opening and re-contact of the cracked surfaces during the cyclic shear sliding.

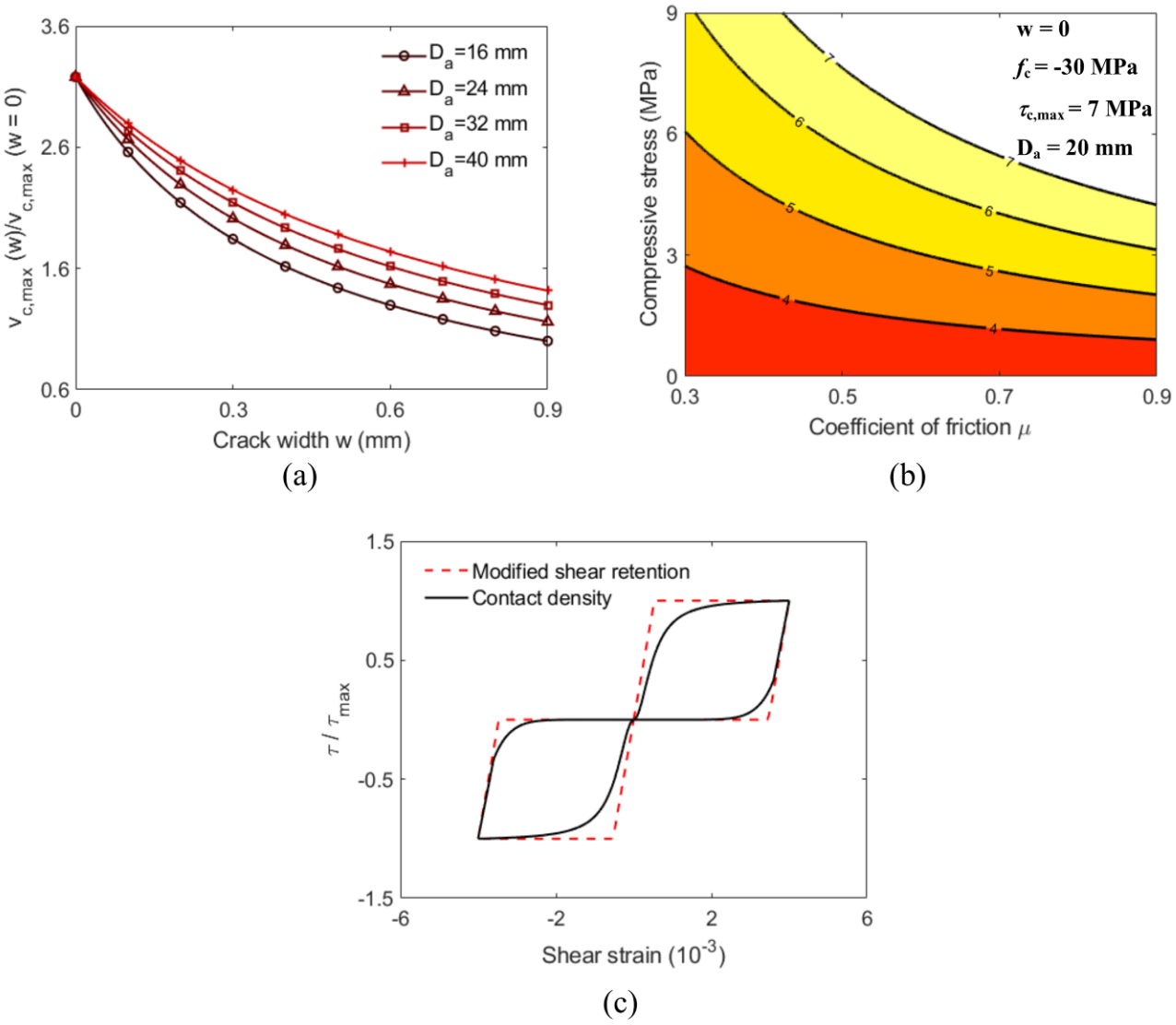

Fig. 4. Shear behaviour across a crack: (a) maximum attainable shear stress ($f_c' = 30$ MPa, $\sigma_1 = 0$ MPa); (b) coupling with normal stress; (c) cyclic responses described by the modified shear retention and contact density model [35].

Equivalent axial strain transformation

In displacement-based numerical analysis, the deformation gradient or stain increments are given at each element integration point at a time step. The total normal strain increment $\delta\bar{\varepsilon}_{ii}$ $(i = 1,2,3)$ of an element cannot be directly used to calculate the uniaxial stresses with Eqs. (6)-(9). The strain increment due to Poisson's effect shall be eliminated to obtain the equivalent uniaxial strain increments $\delta\varepsilon_{ii}$ [37] as

$$\delta\bar{\varepsilon}_{ij} = \delta\varepsilon_{ij} - \sum_{m=1}^{3} \nu_{im}\delta\varepsilon_{mj}\left(1 - \delta_{mj}\right) \qquad (i = j) \tag{23a}$$

$$\delta\bar{\varepsilon}_{ij} = \delta\varepsilon_{ij} \qquad (i \neq j) \tag{23b}$$

The transformation can be expressed as

$$\delta\bar{\boldsymbol{\varepsilon}} = \boldsymbol{\mathcal{L}} \cdot \delta\boldsymbol{\varepsilon} \tag{24a}$$

$$\text{or} \quad \begin{bmatrix} \delta\bar{\varepsilon}_{11} \\ \delta\bar{\varepsilon}_{22} \\ \delta\bar{\varepsilon}_{33} \\ \delta\bar{\varepsilon}_{12} \\ \delta\bar{\varepsilon}_{23} \\ \delta\bar{\varepsilon}_{31} \end{bmatrix} = \begin{bmatrix} 1 & -\nu_{12} & -\nu_{13} & & & \\ -\nu_{21} & 1 & -\nu_{23} & & \mathbf{0} & \\ -\nu_{31} & -\nu_{32} & 1 & & & \\ & & & 1 & 0 & 0 \\ & \mathbf{0} & & 0 & 1 & 0 \\ & & & 0 & 0 & 1 \end{bmatrix} \begin{bmatrix} \delta\varepsilon_{11} \\ \delta\varepsilon_{22} \\ \delta\varepsilon_{33} \\ \delta\varepsilon_{12} \\ \delta\varepsilon_{23} \\ \delta\varepsilon_{31} \end{bmatrix} \tag{24b}$$

and the inverse of Eq. (24) is

$$\begin{bmatrix} \delta\varepsilon_{11} \\ \delta\varepsilon_{22} \\ \delta\varepsilon_{33} \\ \delta\varepsilon_{12} \\ \delta\varepsilon_{23} \\ \delta\varepsilon_{31} \end{bmatrix} = \frac{1}{|\mathcal{L}|} \begin{bmatrix} 1 - \nu_{32}\nu_{23} & \nu_{12} + \nu_{13}\nu_{32} & \nu_{13} + \nu_{12}\nu_{23} & & & \\ \nu_{21} + \nu_{31}\nu_{23} & 1 - \nu_{13}\nu_{31} & \nu_{23} + \nu_{21}\nu_{13} & & \mathbf{0} & \\ \nu_{31} + \nu_{21}\nu_{32} & \nu_{32} + \nu_{12}\nu_{31} & 1 - \nu_{12}\nu_{21} & & & \\ & & & |\boldsymbol{\mathcal{L}}| & 0 & 0 \\ & \mathbf{0} & & 0 & |\boldsymbol{\mathcal{L}}| & 0 \\ & & & 0 & 0 & |\boldsymbol{\mathcal{L}}| \end{bmatrix} \begin{bmatrix} \delta\bar{\varepsilon}_{11} \\ \delta\bar{\varepsilon}_{22} \\ \delta\bar{\varepsilon}_{33} \\ \delta\bar{\varepsilon}_{12} \\ \delta\bar{\varepsilon}_{23} \\ \delta\bar{\varepsilon}_{31} \end{bmatrix} \tag{25}$$

where $|\boldsymbol{\mathcal{L}}| = 1 - \nu_{32}\nu_{23} - \nu_{12}\nu_{21} - \nu_{13}\nu_{31} - \nu_{12}\nu_{23}\nu_{31} - \nu_{21}\nu_{32}\nu_{13}$.

The Poisson' ratio of uncracked concrete is isotropic $\nu_{ij} = \nu_c$. The cracked concrete becomes an anisotropic material and, if the crack is opening in $\mathbf{V}_i^c$ that $\delta\varepsilon_i > 0$, the lateral strain to the axial strain

ratios can be represented by the following empirical relations, which are based on the Hsu/Zhu ratio [30,48] derived from panel tests:

$$\nu_{ij} = \nu_{\rm cr} = \min\left[0.2 + 850\max(|\varepsilon_{sl}|, |\varepsilon_{st}|), \nu_{\rm cr,max}\right] u\left(\sigma_{T3,j} - \sigma_{\rm j}\right) \tag{26a}$$

$$\nu_{ji} = 0.0 \tag{26b}$$

Hence, the crack opening/strain in $\mathbf{V}_i^c$ will not induce lateral strains in $\mathbf{V}_j^c$, meanwhile the axial strain in $\mathbf{V}_j^c$ (if uncracked) will incur higher lateral strains in $\mathbf{V}_i^c$ with $\nu_{ij} > 0.2$ up to $\nu_{\rm cr,max}$. Under cyclic loading and monotonic axial loading, $\nu_{\rm cr,max}$ = 1.0 and 1.9 were recommended respectively [48]. Under torsion loading, ν_{ij} could be reduced by 20% [57]. Therefore, Eq. (24) depends on the largest steel strain of $|\varepsilon_{sl}|$ or $|\varepsilon_{st}|$ in the longitudinal or transverse direction, which controls the crack width and spacing as calculated by Eqs. (15) & (16). The steel strains $|\varepsilon_{sl}|$ and $|\varepsilon_{st}|$ can be taken as the total normal strains of the concrete element along the orientations of the longitudinal and transverse rebar respectively. **Fig. 5** illustrates the crack conditions and the corresponding modified Hsu/Zhu ratios.

The unit step function $u\left(\sigma_{T3,j} - \sigma_j\right) = 1$ if $\sigma_{T3,j} - \sigma_j > 0$ else $u\left(\sigma_{T3,j} - \sigma_j\right) = 0$ is added to the original relation of the Hsu/Zhu ratio to account for the effect of crack opening/closure under cyclic loading. $\sigma_{T3,j}$ is the stress on the crack plane j at the stiffness unilateral point T3 ($\varepsilon_{T2}/3$, $-0.2\alpha_{CD}f_r$) defined in **Fig. 2**. Therefore, the recovery of the ratio will conform to the complete crack closure from tension to compression. Furthermore, the transformation of Eq. (26) with Eq. (27) will lead to a non-symmetric stiffness matrix. And the principal stress and principal strain directions of a material deforming inelastically with a non-symmetric stiffness matrix would certainly be non-coincident.

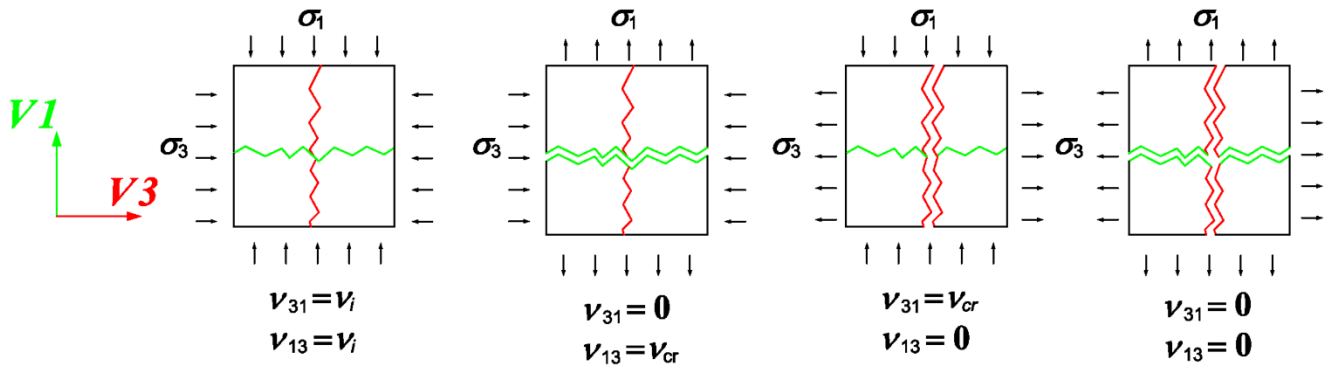

Fig. 5. Poisson's effects under different stress states.

3. Numerical implementation and model behaviour

The numerical implementation of the proposed constitutive model and the development of a novel crack-plane searching algorithm are firstly discussed in section 3.1. Then, in section 3.2, the constitutive behaviour depicted by the proposed model is firstly illustrated by four examples: (1) axial and lateral responses under uniaxial loading, (2) multiaxial responses, (3) shear responses under normal constraints, and (4) general responses under non-proportional loading. In section 3.3, a method for regularising the model parameters according to the element size is proposed for mitigating the mesh-sensitive issues. Lastly, the simulated structural responses of shear panels are presented and compared with the test results in section 3.4.

3.1 Crack plane searching and solution algorithm

The proposed constitutive model has been implemented into ABAQUS using the subroutine for user materials [58]. **Table 1** lists the material parameters and the state variables of the proposed constitutive model. The flowchart of the solution algorithm as described in section 2 is outlined in **Fig. 6**. The constitutive model of the cracked concrete is formulated in terms of total strains and loading-history

dependent state variables. Each state variable has explicit mechanical meaning and can therefore be calibrated using standard material tests. Another essential feature of the proposed model is the eigenvalue decomposition to determine the crack directions based on Eq. (5) criteria. As long as two crack directions are fixed, then the remaining potential crack direction can be determined by orthogonal condition.

Yet, if only one crack direction, say $\mathbf{V_1^c}$, is known, the other two crack directions $\mathbf{V_2^c}$ & $\mathbf{V_3^c}$ cannot be fixed, although they must lie on a unique plane $\wp_\mathbf{1}$ with $\mathbf{V_1^c}$ as the normal vector. Assume that the first crack denoted by script 'c1' is formed in $\mathbf{V_1^c}$ at time t_{c1}, the other eigendirections at the same instance are $\mathbf{V_2}(t_{c1})$ & $\mathbf{V_3}(t_{c1})$. The shear stress may exist on $\wp_\mathbf{1}$ upon subsequent loading and the eigendirections of the stress tensor at a later time shall be deviated from $\mathbf{V_2}(t_{c1})$ & $\mathbf{V_3}(t_{c1})$. To fix $\mathbf{V_2^c}$ & $\mathbf{V_3^c}$ upon subsequent loading, local eigenvalue decomposition on $\wp_\mathbf{1}$ will be performed. The operations are described below.

Firstly, the eigenvectors are stored in columns of a matrix $\mathbf{V}(t_{c1}) = [\mathbf{V_1^c}(t_{c1}), \mathbf{V_2}(\mathrm{t_{c1}}), \mathbf{V_3}(\mathrm{t_{c1}})]$ with $\sigma_1 > \sigma_2 > \sigma_3$ after the first crack occurs at t_{c1}. The second crack denoted by script 'c2' occurs at a later time $t_{c2} > t_{c1}$. The global stress tensor $\tilde{\boldsymbol{\sigma}}(t_{c2})$ is rotated to the frame spanned by $\mathbf{V}(t_{c1})$ as

$$\mathbf{V^T}(t_{c1}) \cdot \tilde{\boldsymbol{\sigma}}(t_{c2}) \cdot \mathbf{V}(t_{c1}) = \boldsymbol{\sigma}(t_{c2}) \tag{27}$$

Then, the local stress $\tilde{\boldsymbol{\sigma}}_{\wp_\mathbf{1}}$ on the plane $\wp_\mathbf{1}$ can be extracted by

$$\tilde{\boldsymbol{\sigma}}_{\wp_\mathbf{1}} = \mathcal{R} \cdot \boldsymbol{\sigma}(t_{c2}) \cdot \mathcal{R} \tag{28}$$

The eigenvalue decomposition of $\tilde{\boldsymbol{\sigma}}_{\wp_\mathbf{1}}$ on the plane $\wp_\mathbf{1}$ is then performed

$$\mathbf{V}_{\wp_\mathbf{1}}^{\boldsymbol{T}}(t_{c2}) \cdot \tilde{\boldsymbol{\sigma}}_{\wp_\mathbf{1}} \cdot \mathbf{V}_{\wp_\mathbf{1}}(t_{c2}) = \boldsymbol{\sigma}_{\wp_\mathbf{1}} \tag{29}$$

where $\mathcal{R}$, $\tilde{\boldsymbol{\sigma}}_{\wp_\mathbf{1}}$ & $\mathbf{V}_{\wp_\mathbf{1}}(t_{c2})$ have the following forms:

$$\mathcal{R} = \begin{bmatrix} 0 & 0 & 0 \\ 0 & 1 & 0 \\ 0 & 0 & 1 \end{bmatrix};\ \tilde{\boldsymbol{\sigma}}_{\boldsymbol{\wp_1}} = \begin{bmatrix} 0 & 0 & 0 \\ 0 & \sigma_{22} & \sigma_{23} \\ 0 & \sigma_{32} & \sigma_{33} \end{bmatrix};\ \mathbf{V}_{\boldsymbol{\wp_1}} = \begin{bmatrix} 1 & 0 & 0 \\ 0 & V_{\wp_1}^{22} & V_{\wp_1}^{23} \\ 0 & V_{\wp_1}^{32} & V_{\wp_1}^{33} \end{bmatrix} \tag{30}$$

The 2D plan $\boldsymbol{\wp_1}$ is spanned by the eigenvectors $\mathbf{V}_{\wp_1}^2 = \left[0, V_{\wp_1}^{22}, V_{\wp_1}^{32}\right]^T$ & $\mathbf{V}_{\wp_1}^3 = \left[0, V_{\wp_1}^{23}, V_{\wp_1}^{33}\right]^T$ in the local coordinates. As far as one of the eigenvalues $\boldsymbol{\sigma}_{\boldsymbol{\wp_1}}$ satisfy the condition of Eq. (5), the directions of crack planes $\mathbf{V}_{\mathrm{C}} = [\mathbf{V_1^c}, \mathbf{V_2^c}, \mathbf{V_3^c}]$ in the global coordinates can be obtained by left-multiplying $\mathbf{V}_{\boldsymbol{\wp_1}}$ with $\mathbf{V}$:

$$\mathbf{V}_{\mathrm{C}} = \mathbf{V}(t_{c1}) \cdot \mathbf{V}_{\boldsymbol{\wp_1}}(t_{c2}) \tag{31}$$

In the subsequent loading or a new time step, $\mathbf{V}_{\mathrm{C}}$ will be used to rotate the global strain tensors to the cracked plane coordinates, where the stress increments and the changes of state variables are evaluated. It should be noted that $\mathbf{V}_{\mathrm{C}}$ denote the normal directions of the stored crack planes and the corresponding normal stress $\boldsymbol{\sigma}_{\mathrm{C}} = [\sigma_1^c, \sigma_2^c, \sigma_3^c]$ would not be in the same order as the principal stresses such as $\sigma_1 > \sigma_2 > \sigma_3$.

If all cracks are formed due to the exceedance of tensile strength in a principal stress direction, the crack coordinate can be uniquely defined. However, if a crack plane with the opening direction $\mathbf{V_1^c}$ is caused by the principal compressive stress in $\mathbf{V_3}(t_{c1})$ at t_{c1}, additional constraints on the subsequent crack formation are needed to ensure a unique crack coordinate. The principal compression direction $\mathbf{V_3}(t' > t_{c1})$ at time t' may deviate from $\mathbf{V_3}(t_{c1})$ at time t_{c1} if a shear stress τ_{13} occurs on the crack plane $\mathbf{V_1^c}$. Yet, owing to the orthogonal constraint, the principal compressive stress in $\mathbf{V_3}(t')$ shall not incur a new crack plane other than $\mathbf{V_1^c}$, provided that $\mathbf{V_3}(t')$ is not perpendicular to $\mathbf{V_3}(t_{c1})$ and the first crack in V_1^c remains open. A particular case is that when the first crack $\mathbf{V_1^c}$ is closed at t and the normal stress on the crack plane $\sigma_1^c(t')$ becomes less than the maximum principal stress $\sigma_1(t')$, then a new crack plane will form in $\mathbf{V_2}(t' > t_{c1})$ if $\sigma_3(t') = c_{\mathrm{ck}}\xi f_c$ (Eq. 5(b)).

Table 1. Model parameters and essential state variables.

Attribute	Description	Equation(s)
Model parameters, $\mathbb{C}_m$		
E_c, ν_c, G_c	Young's modulus, Poisson's ratio, and shear modulus respectively of uncracked concrete	(9), (21), (24)
f_c, f_r	Uniaxial compressive strength and uniaxial tensile strength respectively	(6), (9)
ε_o, ε_r	Corresponding strains at f_c and f_r respectively	(6), (9)
b_{C}	The ratio between the plastic strain and the cracking strain in compression	(11)
ψ	Control the effect of cyclic damage on the compressive strength	(7)
a_c a_t	Govern the decay of the compressive and tensile stress respectively after the peak	(6), (9)
D_a	Maximum aggregate size	(14)
β_v	Shear retention factor	(21)
ρ_{el}, ρ_{et}	Reinforcement ratios of the longitudinal rebar and transverse rebar respectively	(17)
μ	Coefficient of friction for the shear transfer across a crack	(18), (19)
c_{ck}	The ratio of the crack strength to the peak strength under compression	(4), (5)
$\nu_{\mathrm{cr,max}}$	The maximum Hsu/Zhu ratio	(26)
State variables, $\mathbb{Z}_n$		
$\mathbf{V_j}$, $\breve{\mathbf{V}}_\mathbf{j}$	Principal directions of the stress tensor and the strain tensor respectively	(1) & (2)
$\mathbf{V_j^c}$	The normal vector of the j[th] crack plane	(5)
$\tilde{\boldsymbol{\sigma}}$, $\boldsymbol{\sigma}$	Stress tensors in the global Cartesian coordinate and the crack plane coordinate respectively	(1) & (2)
$\tilde{\boldsymbol{\varepsilon}}$, $\bar{\boldsymbol{\varepsilon}}$	Strain tensors in the global Cartesian coordinate and the crack plane coordinate respectively	(1) & (2)
$\boldsymbol{\varepsilon}$	Equivalent strain tensor	(21)
D_i [#]	Control the compressive strength softening due to cyclic loading	(7)
ζ_i	Control the compressive strength softening due to the orthogonal tensile strain and concrete strength	(8)
$\varepsilon_{\mathrm{C2}i}$, f_{c2i}	Strain and stress at the load reversal point C2 from the compression envelope	Figure X1 (a)
$\varepsilon_{\mathrm{C4i}}$, $f_{c4(i)}$	Strain and stress at the load reversal point C4 that already passed through C3 from tension to compression	Figure X1 (a)
$\varepsilon_{\mathrm{T2}i}$, f_{T2i}	Strain and stress at the load reversal point T2 from the tension envelope	Figure X1 (b)
α_{CDi}	Stress reduction factor for the unilateral points T3 and T4 where the abrupt change of stiffness occur	(11)
$\hat{\tau}_{ci}$, $\tau_{ci,max}$	The maximum shear stress on the crack plane under the absence or the presence of normal compression respectively	(14) & (1)
L_{cs}	Crack spacing along the crack extension direction	(16)
ρ_{e1}	Effective reinforcement ratio along the crack extension direction	(17)
ν_{ij}	Effective Poisson's ratio after cracking	(24) –(27)

[#] i = 1, 2, 3 denote that the state variable is stored for the first, second, or third crack plane respectively.

Hence, a second crack plane shall only form if the conditions (**Fig. 7**) given by Eq. (32) are satisfied. This condition is trivial for 2D elements but is necessary for 3D elements since the crack coordinate cannot be fixed until the second crack plane occurs.

$$\mathbf{V_2^c}(t_{c1}) = \mathbf{V_2}(t' > t_{c1}) \quad \text{if } \sigma_3(t') = c_{\mathrm{ck}}\xi f_c \text{ and } \begin{cases} \mathbf{V_3}(t_{c1}) \cdot \mathbf{V_3}(t') = 0 \\ \mathbf{V_3}(t_{c1}) \cdot (t') \neq 0 \text{ with } \sigma_1^c(t') < 0 \;\&\; \neq \sigma_1(t') \end{cases} \tag{32}$$

Similar conditions are adopted to determine the formation of the third crack, although $\mathbf{V_3^c}$ is already uniquely fixed after the determination of $\mathbf{V_1^c}$ & $\mathbf{V_2^c}$ based on the orthogonal condition.

3.2 Simulated three-dimensional constitutive behaviour

As demonstrated in section 2, the cyclic stress-strain behaviour under uniaxial loading on the crack plane that involves significant material softening can be simulated without difficulties. This section further examines if the proposed model's multiaxial constitutive behaviour can comply with the experimentally observed behaviour discussed above. Unless otherwise specified, the material parameters adopted in the following case studies are based on the mean properties of concrete C20/25 as per Eurocode 2 [59]: $E_c = 29.96\text{GPa}$, $\nu_c = 0.2$, $f_c = -28$ MPa, $f_r = 2.21$ MPa, $\varepsilon_o = -2.0 \times 10^{-3}$, $\varepsilon_r = 7.727 \times 10^{-5}$. Meanwhile, the following parameters are based on the recommendations [10,30,42,53]: $b_{\mathrm{C}} = 0.5$, $\psi = 0$, $a_c = 4$, $D_a = 32$ mm, $\beta_v = 0.2$, $\mu = 0.7$, $c_{\mathrm{ck}} = 0.7$, $\nu_{\mathrm{cr,max}} = 1.0$, $a_t = 1.0$.

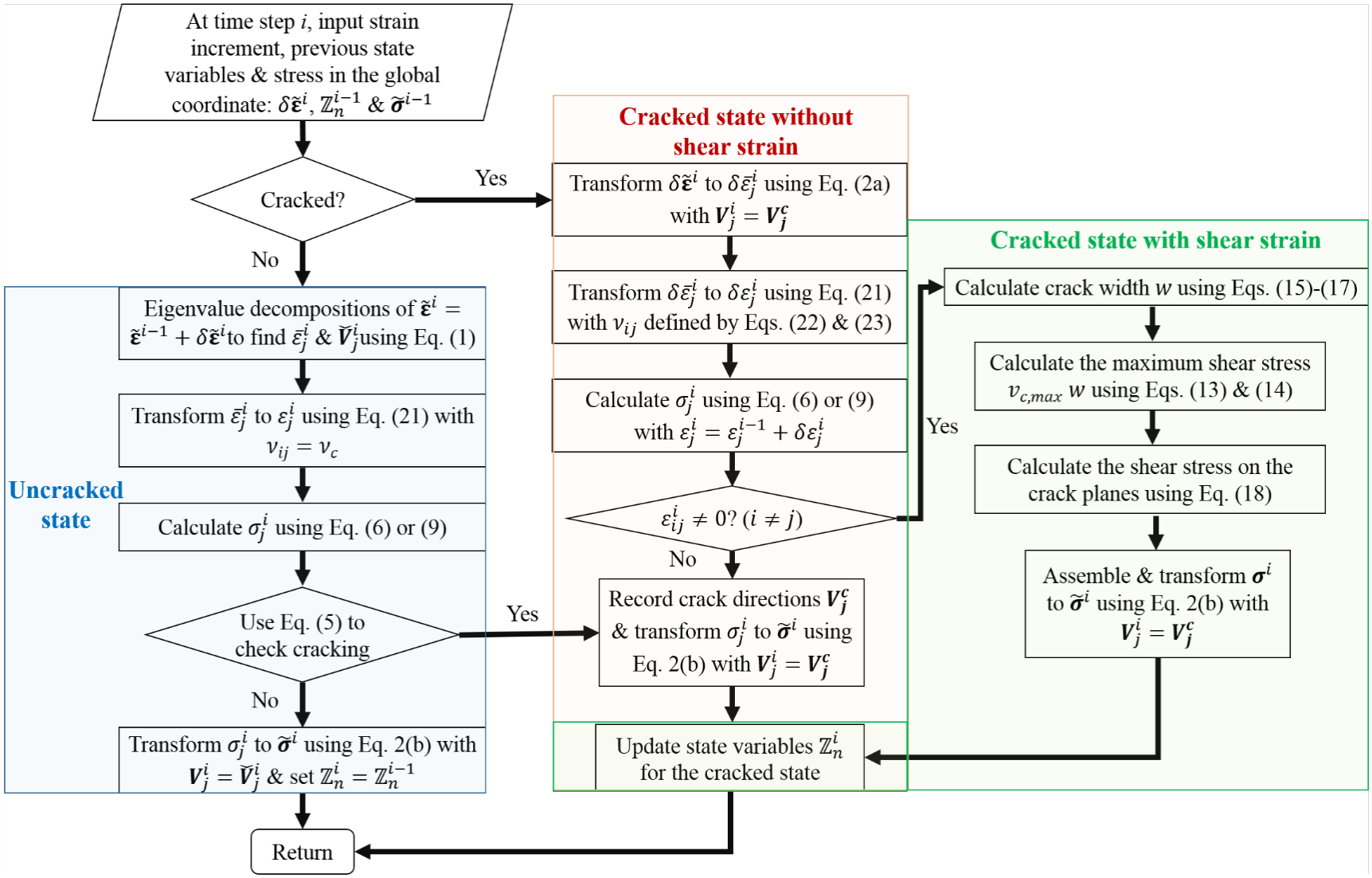
At time step i, input strain increment, previous state variables & stress in the global coordinate: $\delta\tilde{\boldsymbol{\varepsilon}}^i$, $\mathbb{Z}_n^{i-1}$ & $\tilde{\boldsymbol{\sigma}}^{i-1}$
Cracked?
Yes
No
Uncracked state
Eigenvalue decompositions of $\tilde{\boldsymbol{\varepsilon}}^i = \tilde{\boldsymbol{\varepsilon}}^{i-1} + \delta\tilde{\boldsymbol{\varepsilon}}^i$ to find $\bar{\varepsilon}_j^i$ & $\bar{\boldsymbol{V}}_j^i$ using Eq. (1)
Transform $\bar{\varepsilon}_j^i$ to ε_j^i using Eq. (21) with $\nu_{ij} = \nu_c$
Calculate σ_j^i using Eq. (6) or (9)
Use Eq. (5) to check cracking
Yes
No
Transform σ_j^i to $\tilde{\boldsymbol{\sigma}}^i$ using Eq. 2(b) with $\boldsymbol{V}_j^i = \bar{\boldsymbol{V}}_j^i$ & set $\mathbb{Z}_n^i = \mathbb{Z}_n^{i-1}$
Return
Cracked state without shear strain
Transform $\delta\tilde{\boldsymbol{\varepsilon}}^i$ to $\delta\bar{\varepsilon}_j^i$ using Eq. (2a) with $\boldsymbol{V}_j^i = \boldsymbol{V}_j^c$
Transform $\delta\bar{\varepsilon}_j^i$ to $\delta\varepsilon_j^i$ using Eq. (21) with ν_{ij} defined by Eqs. (22) & (23)
Calculate σ_j^i using Eq. (6) or (9) with $\varepsilon_j^i = \varepsilon_j^{i-1} + \delta\varepsilon_j^i$
$\varepsilon_{ij}^i \neq 0?\ (i \neq j)$
Yes
No
Record crack directions $\boldsymbol{V}_j^c$ & transform σ_j^i to $\tilde{\boldsymbol{\sigma}}^i$ using Eq. 2(b) with $\boldsymbol{V}_j^i = \boldsymbol{V}_j^c$
Update state variables $\mathbb{Z}_n^i$ for the cracked state
Cracked state with shear strain
Calculate crack width w using Eqs. (15)-(17)
Calculate the maximum shear stress $v_{c,max}$ w using Eqs. (13) & (14)
Calculate the shear stress on the crack planes using Eq. (18)
Assemble & transform $\boldsymbol{\sigma}^i$ to $\tilde{\boldsymbol{\sigma}}^i$ using Eq. 2(b) with $\boldsymbol{V}_j^i = \boldsymbol{V}_j^c$

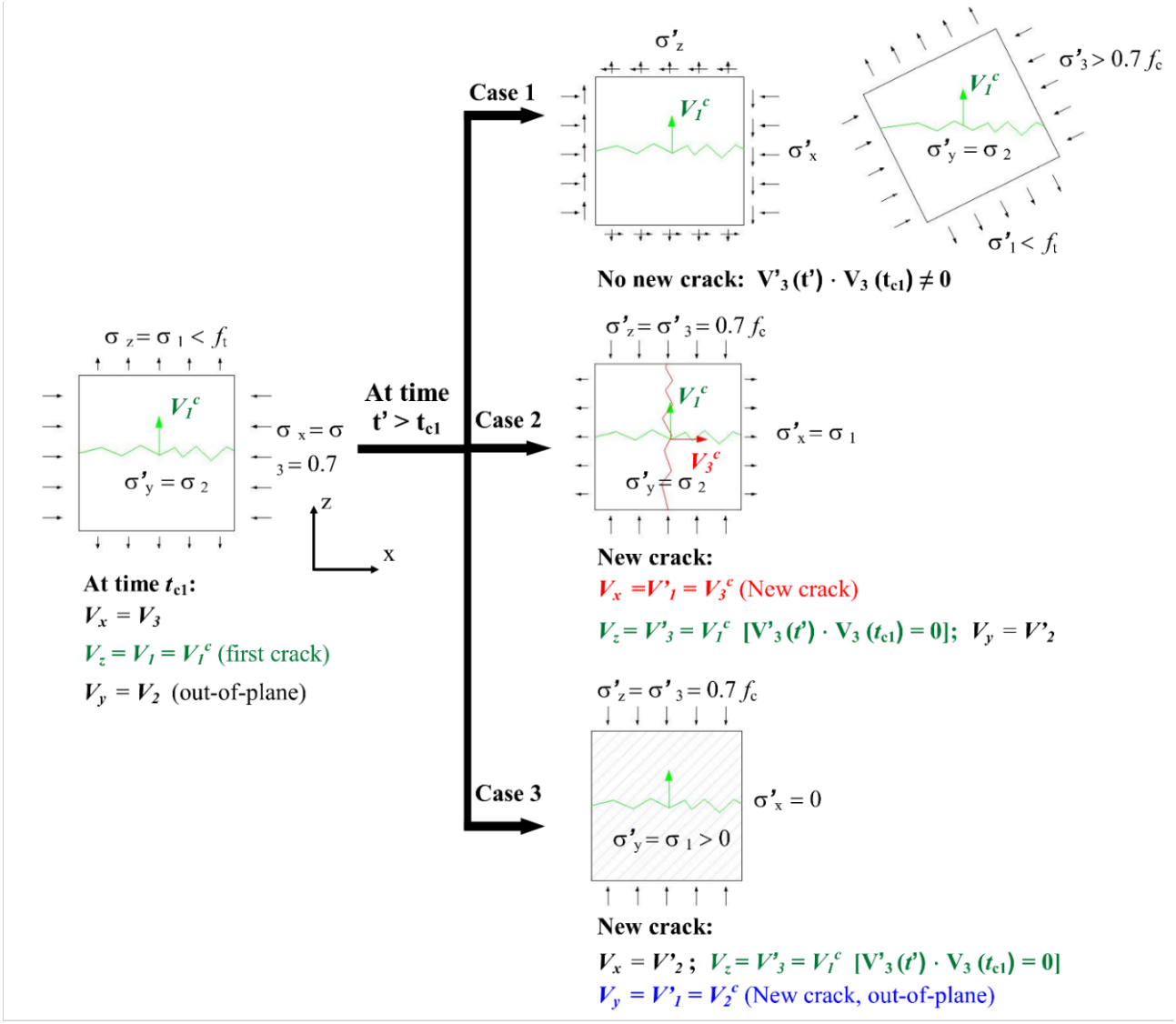

3.2.1 Lateral behaviour under axial loading

Fig. 8(a) presents the simulated evolutions of the axial strain ε_x, lateral strain $\varepsilon_L = \varepsilon_y = \varepsilon_z$, volumetric ε_v and equivalent deviatoric strains ε_D, which are defined by Eqs. (33) and (34) respectively, under the applied compressive stress σ_x. The material parameters adopted are $f_c = -32.8$ MPa and $\varepsilon_o = -2.24 \times 10^{-3}$ based on the test results by Kupfer *et al.* [60], while $\nu_{\mathrm{cr,max}} = 0.8$.

$$\varepsilon_v = \varepsilon_1 + \varepsilon_2 + \varepsilon_3 \tag{33}$$

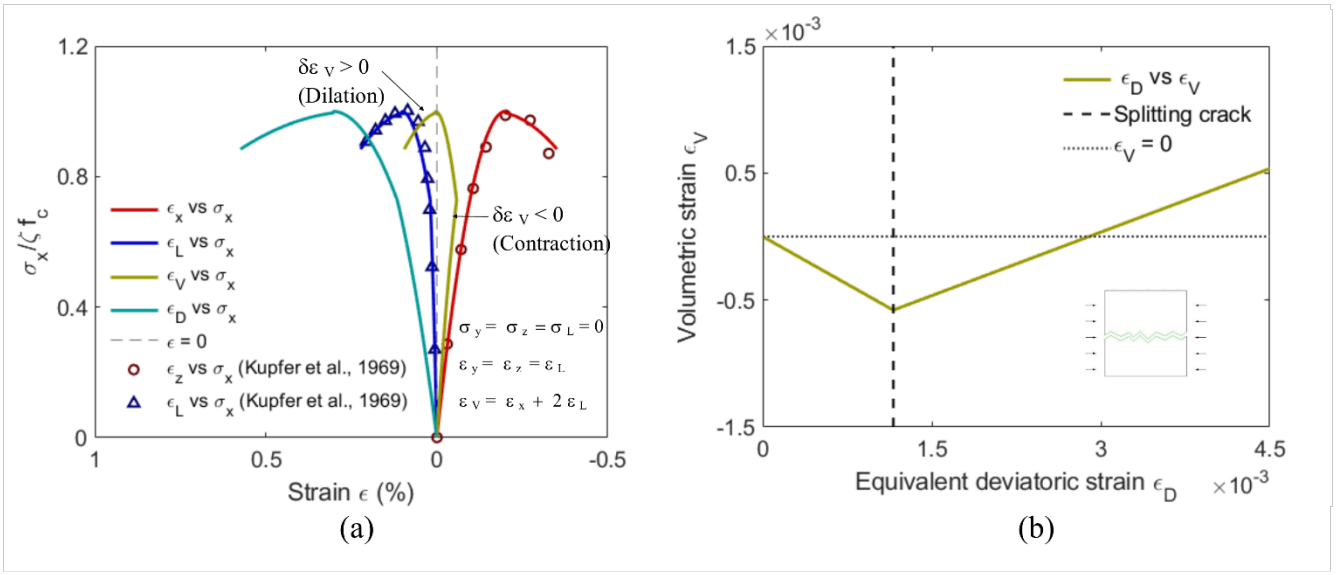

$$\varepsilon_D = \sqrt{\frac{(\varepsilon_1-\varepsilon_2)^2+(\varepsilon_2-\varepsilon_3)^2+(\varepsilon_3-\varepsilon_1)^2}{2}} \tag{34}$$

where ε_1, ε_2, ε_3 are the principal strains.

When concrete is compressed beyond the elastic state, dilation $\varepsilon_v > 0$ occurs [8] due to the initiation and propagation of the microscopic wing cracks discussed above. The elastic contraction $\varepsilon_v > 0$ due to the regular Poisson's effect with $v_c \leq 0.2$ was terminated when the compressive crack strength $-0.7\zeta f_c$ was exceeded. Afterwards, the Hsu/Zhu ratio v_{ij} (Eq. 26) that governs the ratio between the inelastic lateral and axial strain continued to increase with the total strains, and the dilation begins when $v_{ij} = v_{xz} = v_{yz} > 0.5$. **Fig. 8(b)** shows the evolution of volumetric strain ε_v against the equivalent deviatoric strain ε_D.

3.2.2 Reversed axial loading with lateral constraints

Fig. 9 presents the simulated multiaxial stress evolutions under lateral constraints that strains $\bar{\varepsilon}_y$ and $\bar{\varepsilon}_z$ remained constants of -5×10^{-5} and 5×10^{-5} respectively, while increasing compression was applied in x until $\bar{\varepsilon}_x = -1.5 \times 10^{-3}$. Then, the loading was reversed to tension and stopped at $\bar{\varepsilon}_x = 2.5 \times 10^{-3}$. The small strains imposed on y and z were to ensure the principal strains could have different values. The first crack with normal vector $\boldsymbol{V_{c1} = V_z}$ formed, when the compressive stress σ_x exceeded the prescribed crack strength of $-0.7\zeta f_c$**.** Then, the second crack $\boldsymbol{V_{c2} = V_x}$ formed when the stress σ_x was reversed and reached f_r. Before the second crack occurred, the stored normal vectors of the crack or potential crack planes were $\left[\boldsymbol{V_{c1} = V_z, V_y, V_x}\right]$ since $\sigma_z = \sigma_1$, $\sigma_y = \sigma_2$ and $\sigma_x = \sigma_3$. The crack coordinate remained unchanged until the second crack plane formed and the stored crack plane vectors became $\left[\boldsymbol{V_{c1} = V_z, V_{c2} = V_x, V_y}\right]$. Swapping of $\boldsymbol{V_y}$ and $\boldsymbol{V_x}$ in the stored crack vector positions occurred, as the new crack opened in x with $\sigma_x = \sigma_1$ and the xz plane with normal vector $\boldsymbol{V_y}$ remained uncracked. Furthermore, to maintain the total strains $\bar{\varepsilon}_y$ and $\bar{\varepsilon}_z$ unchanged, non-zero σ_z & σ_y, i.e. the equivalent strains $\varepsilon_z \neq 0$ & $\varepsilon_y \neq 0$, were needed such that the total strain changes due to the Poison's effect and stress could counterbalance with each other.

Furthermore, the proposed model can simulate an interesting behaviour related to Poisson's effect before and after the closure of the cracks. When the compressive stress σ_x first reached $-0.7\zeta f_c$, the splitting crack $\boldsymbol{V_{c1} = V_z}$ occurred but was closed initially as the crack plane was under compression $\sigma_z < 0$. Following the loading reversal in x, σ_z increased and eventually became positive. At that point, the crack plane $\boldsymbol{V_{c1}}$ opened and the equivalent strain in the corresponding direction $\varepsilon_{c1} = \varepsilon_z$ increased at a faster rate as shown in **Fig. 9(c),** since the Poisson' effect ν_{zx} as defined by Eq. (26) and illustrated in **Fig. 5** increased upon the crack opening.

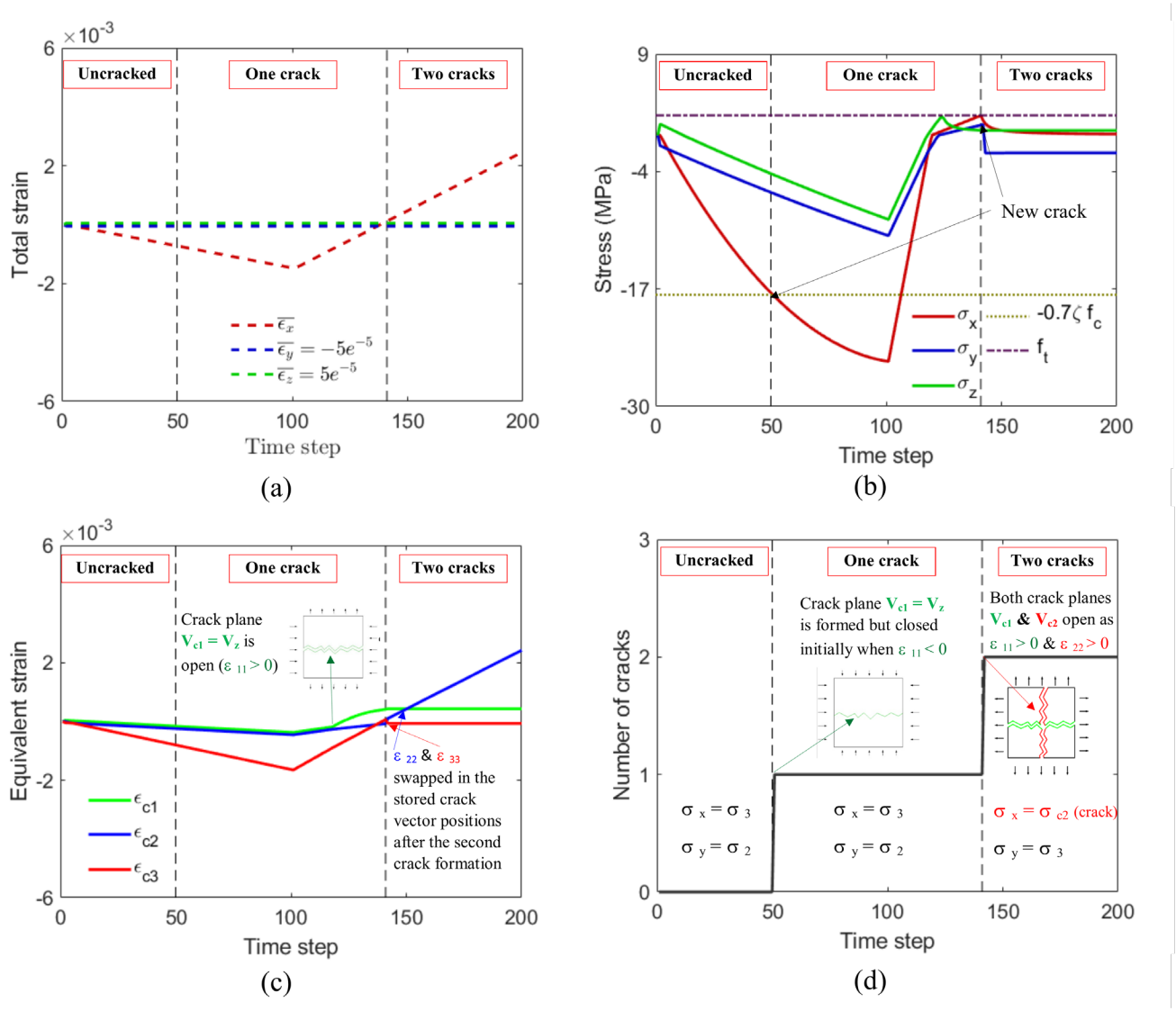

Fig. 9. Multiaxial responses and cracking under reversed axial loading: (a) total normal strains; (b) stress in global coordinate; (c) equivalent normal strains on crack planes; and (d) the number of cracks.

3.2.3 Shear with normal constraints

The simulated responses under planar shear strain γ_{xz} with normal constraints, i.e. $\bar{\varepsilon}_x = \bar{\varepsilon}_z = 0$. are shown in **Fig. 10**. The shear stress-strain curve was unsurprisingly linear until a crack occurred in the maximum principal stress direction σ_1 (45° from the x-axis). If the normal deformations of the element were not constrained, then the shear crack strength would be the peak strength as well. Yet, in this case, the shear stress could increase further due to the confining stresses provided by the normal constraints.

In RC elements without normal constraints, the essential normal stresses are provided by longitudinal and transverse rebar through the so-called "truss mechanisms" [5], allowing the continuous transfer of shear stress in the post-cracking state. The yielding of rebar in the "truss mechanisms" would limit the normal stresses and shear stress. Yet, regardless of the rebar amount, the crushing of the diagonal struts imposes the upper limit of the attainable shear stress, which is a well-known RC behaviour and well captured by the proposed model.

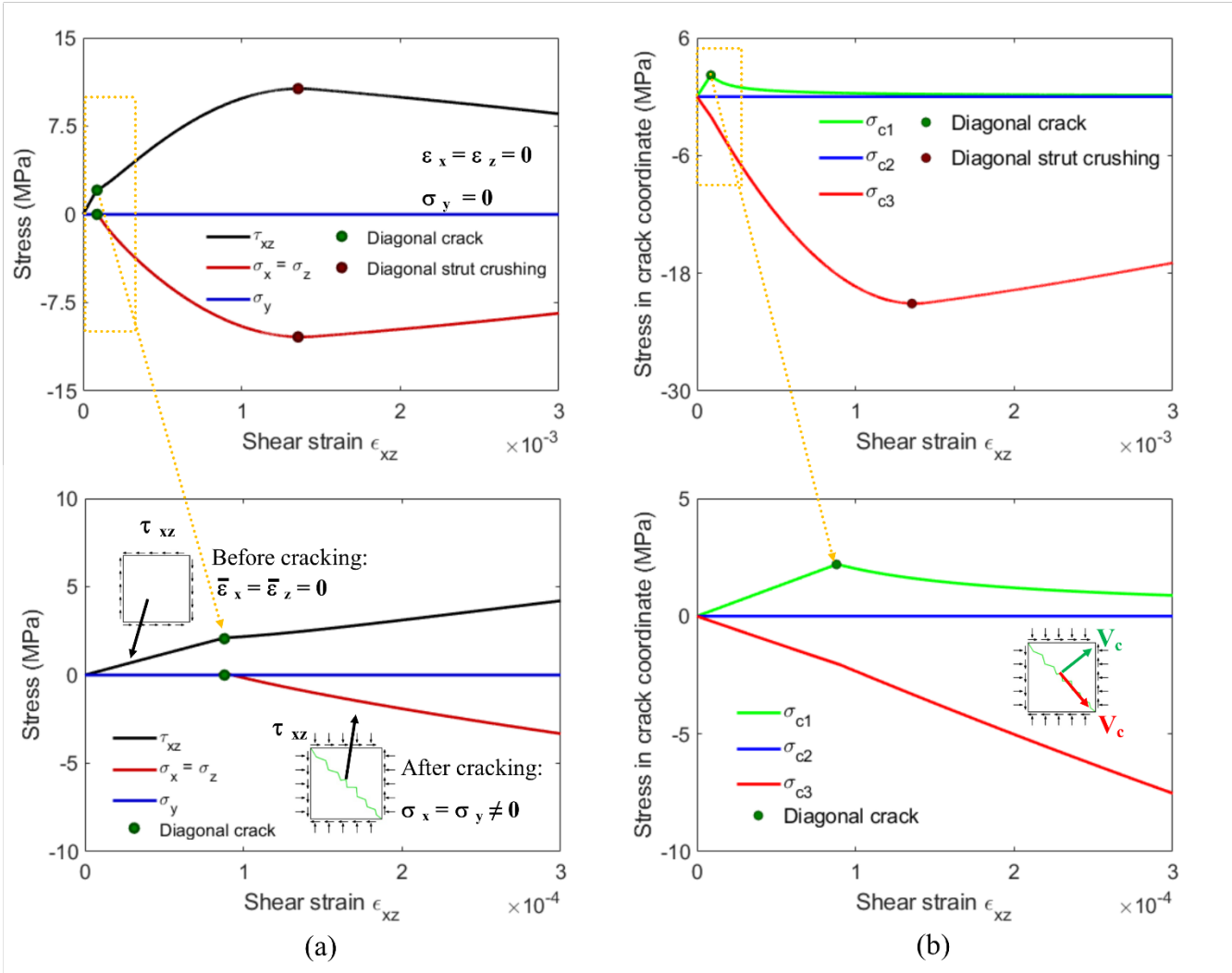

Fig. 10. Shear responses under normal constraints: (a) shear stress-strain behaviour; (b) principal stress responses.

3.2.4 Non-proportional loading

Fig. 11 presents the simulated general behaviour under non-proportional loading. The xz plane was first cracked by the applied tensile loading in $\boldsymbol{V_y = V_{c1}}$**,** then the deformation in y was constrained and reversing normal strains $\bar{\varepsilon}_x$, $\bar{\varepsilon}_z$ and shear strain ε_{xz} were applied**.** The second crack formed at 168.9° from the x-axis (**Fig. 11(e))** due to the exceedance of the tensile strength in $\boldsymbol{V_{c2}}$ (**Fig. 11(d))**. Then, the normal stress on $\boldsymbol{V_{c2}}$ was reversed to compression with increasing magnitude in a later stage. But when σ_{c2} first passed the compressive crack strength, no new crack would form as σ_{c1} is still larger than σ_{c3} at that point and therefore, the splitting direction remained $\boldsymbol{V_{c1}}$ which was cracked in the beginning stage. The third crack formed when $\sigma_{c3} > \sigma_{c1}$ and the crack $\boldsymbol{V_{c1}}$ is closed with $\sigma_{c1} < 0$, then $\boldsymbol{V_{c3}}$ at -101.1 ° from the x-axis was split open (**Fig. 11(e))**.

The first crack and second crack directions coincided with the principal stress directions as intended. However, due to the orthogonal crack-plane constraint, the third crack did not coincide with the principal stress directions. Furthermore, it can be observed in **Fig. 11(f)** that the principal stress and principal strain directions in the xz plane would strictly coincide before any in-plane crack occurs. After cracking in $\boldsymbol{V_{c2}}$, the induced shear stress on the crack plane leads to the principal stress directions gradually deviating from the principal strain directions. In particular, a significant deviation occurred when the loading direction was reversed. Therefore, the principal stress and strain directions are generally non-coincident under non-proportional loading. Furthermore, an interesting sudden stress decrease (compressive stress increased) in $\boldsymbol{V_{c1}}$ occurred near the very end of the loading stage, as shown in **Fig. 11(d)**. This event corresponded to the closure of the crack in $\boldsymbol{V_{c1}}$ when $\varepsilon_{c1} < 0$ as shown in **Fig. 11(b)**. In summary, the intended behaviour, including the crack formations, crack opening and closure effects, shear stress effects on cracks, and non-coincidence of principal stress and strain directions could be adequately captured by the proposed model.

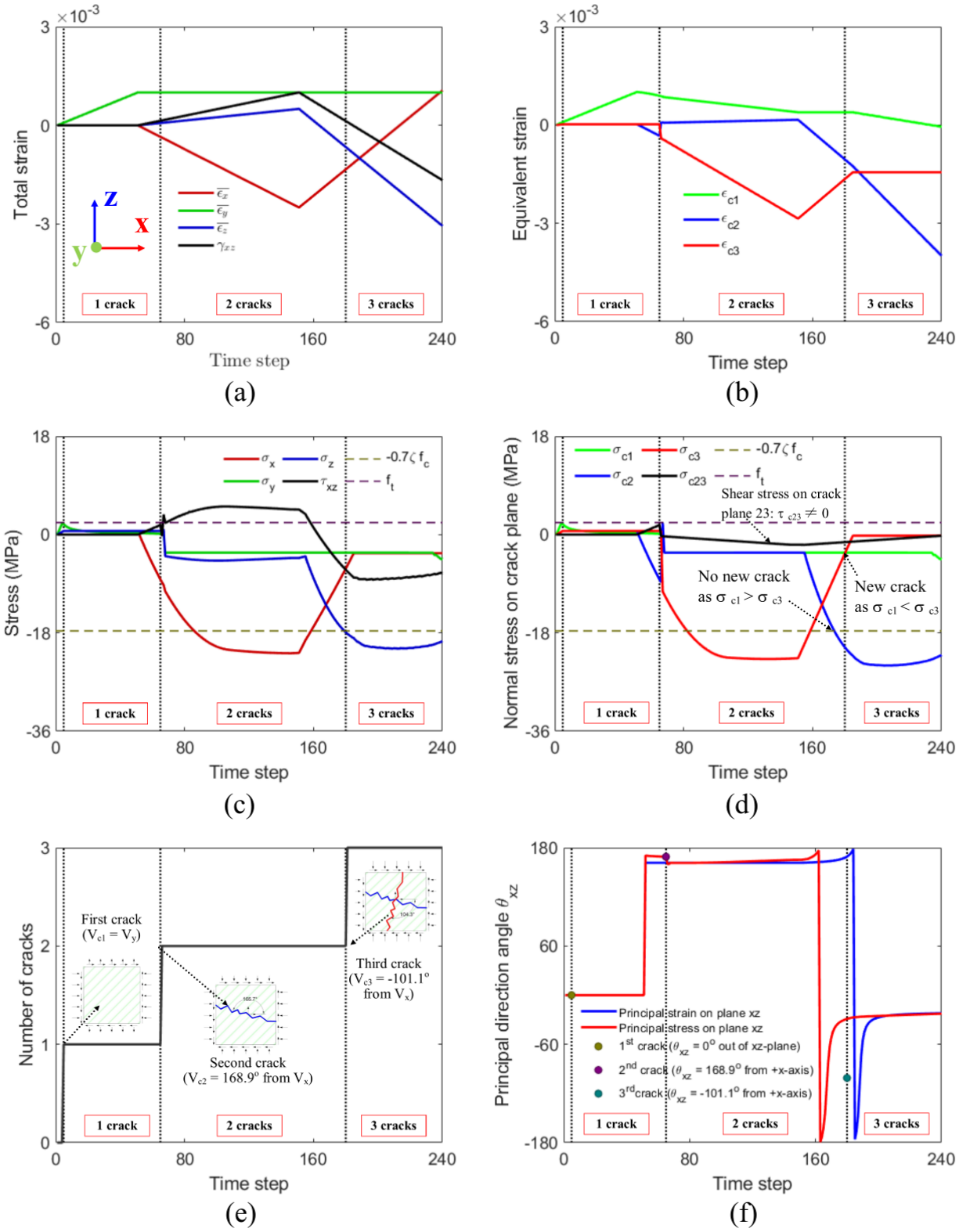

Fig. 11. Responses under non-proportional loading: (a) total strain; (b) equivalent normal strains on crack planes; (c) stresses in the regular coordinate; (d) stresses in the crack plane coordinate; (e) number of cracks; (f) principal stress and strain directions.

3.3 Mitigating mesh-sensitivity and mesh size restrictions

Mesh sensitivity in continuum finite element analysis would be resulted from the softening stress-strain curves due to the localised inelastic deformation [10,39,61] that can significantly affect the simulated post-peak structural responses. To reduce the mesh sensitivity, the descending branches of the stress-strain curves (6b) and (9b) shall be dependent on the mesh size or the element characteristic length [58]. A convenient method to mitigate the mesh-sensitivity is by using the tested stress-displacement curves, and the equivalent strain can be obtained by dividing the displacement δ with the element characteristic length l_e, over which the inelastic deformation in the actual damage or fracture process zone is smeared. Another method is to adjust the decay rate of the descending branches based on the element characteristic length [10,39] or the width of the crack/damage band [62]. Contrasting to the hardening system with elements undergoing homogenous deformation, softening elements will experience localised deformation, and their neighbouring elements will experience elastic unloading. The dissipation, which can be evaluated by integrating the element stress over the displacement, will occur locally in the softening elements. If the stress-strain model remains unchanged, change of the element size will lead to different element dissipation upon softening at a given element displacement, which is the cause of the mesh-sensitivity issues. Therefore, the decay rate of the softening stress-strain curves shall be made element-size dependent such that systems of different mesh sizes can achieve similar dissipation. Integrating Eqs. (9b) and (6b) with respect to the post-peak displacement with $\delta = \varepsilon l_e$ and excluding the strength modification factors, we have

$$\Theta_t = \int_{\delta_r(\sigma_t=f_r)}^{\infty(\sigma_t=0)} f_r \left(\frac{\delta_r}{\delta_1}\right)^{a_t} d\delta_1 = \frac{f_r^2 l_e}{E(a_t-1)} \tag{35}$$

$$\Theta_c = \int_{\delta_o(\sigma_c=f_c)}^{\delta_u(\sigma_c=0)} f_c \left[1 - \left(\frac{\delta_3/\delta_o - 1}{a_c - 1}\right)^2\right] d\delta_3 = \frac{2}{3} f_c \delta_o (a_c - 1) \tag{36}$$

For the evaluation of Eq. (36), the relationship $\delta_u = a_c\delta_o$ when $\sigma_c = 0$ was used. As $\varepsilon_1 l_e$ can be regarded as the crack opening displacement, Θ_t is equivalent to the mode I fracture energy G_t [62]. From Eq. (35), a_t can be directly evaluated as

$$a_t = 1 + \frac{f_r^2 l_e}{EG_t} = 1 + \frac{l_e}{l_{ft}} \tag{37}$$

in which $l_{ft} = EG_t/f_r^2$ is commonly known as the characteristic length of fracture [63]. If the element size is too large, the snap-back phenomenon and the material softening may occur [10,62]. The element size of $l_e \leq l_{ft}$ was recommended [62] to avoid the snap-back. The fracture energy of normal strength concrete can be estimated according to CEB-FIP Model Code 2010 [53]

$$G_t = 0.073 f_c^{0.18} \qquad \text{(in N, mm)} \tag{38}$$

It can be seen that a_t must be larger than 1; otherwise, the integration of Eq. (35) is divergent.

Following [10,47], the localised crushing energy G_c relevant to the softening branch is estimated as:

$$G_c \approx \Theta_c + \frac{1}{2}\mathrm{f}_c\delta_o(1 - b_c) = \frac{2}{3}f_c\delta_o(a_c - 1) + \frac{1}{2}\mathrm{f}_c\delta_o(1 - b_c) \tag{39}$$

For the consistency of the localised crushing energy by the elements, the following condition is enforced using Eq. (36) and $\delta_o = \varepsilon_o l_e$

$$G_c = \frac{f_c\varepsilon_o l_e}{3}\left[2a_c - \frac{3b_c+1}{2}\right] \tag{40}$$

Rearranging Eq. (40) for a_c, we have

$$a_c = \mathcal{H} + \frac{3b_c+1}{4} \tag{41}$$

where

$$\mathcal{H} = \frac{3G_c}{2f_c\varepsilon_o l_e} \tag{42}$$

Similarly, the element length is restricted as below to prevent snap-back behaviour under compression:

$$l_e \leq l_{fc} = \frac{G_c}{f_c\varepsilon_o} \tag{43}$$

Uniaxial compressive stress-strain behaviour of concrete is often determined from compressive tests on the cylindrical specimen. In the original model, $a_c = 4$ [30] can be regarded as the test result from the standard uniaxial compressive tests. But the length of the compressive fracture process zone l_{cp} would not spread over the whole specimen and it can be estimated using the following equation [47]

$$l_{cp} = \frac{1300}{\sqrt{f_c}} \qquad \text{(in mm, MPa)} \tag{44}$$

For instance, the localised crushing energy of grade C30 concrete with $\varepsilon_o = 0.0023$, and $f_c = 30\text{MPa}$ [53] can be calculated by Eq. (42) with $l_e = l_{cp} = 237\ \text{mm}$ and Eq. (39) that gives $G_c = 46.6\ \text{N/mm}$. Furthermore, the element size should be smaller than the expected crack spacing L_{cs} given by Eq. (16) such that no more than one crack or damage process would be contained in each element. Therefore, the element size shall be limited as follows

$$\min\left(l_{ft},\ l_{fc},\ L_{cs}\right) > l_e \tag{45}$$

3.4 Shear panel tests

Shear panel tests are the most classical tests used to verify the multiaxial constitutive models for concrete under pure shear. Shear panels A4, B4, B5, and B6 tested by Pang and Hsu [64] and panel SE6 tested by Kirschner and Collins [65] are simulated with the proposed models. Unlike the typical approach of simply generating the shear stress-strain curves for specific reinforcing ratios [28], the panel tests were simulated by structural FEM models, and the averaged shear stress-strain curves are calculated from the

load-deformation responses. The reinforcing bars were modelled with linear beam elements and embedded in the concrete 3D elements. Elastic perfectly plastic stress-strain relationships were assumed for the rebar. The concrete compressive strength is $f_c = -42.6$ MPa, and the yield strength of the rebar is $f_y = 470$ MPa. The mesh size is 50 mm, and the corresponding mesh-size dependent parameters are determined according to the aforementioned method. The panels have the same reinforcing ratio in the vertical direction $\rho_z = 2.96\%$ but the varying reinforcing ratio in the horizontal direction. As shown in **Fig. 12**, the simulated responses can match the tested results well. The increase of the reinforcing ratios leads to decreased extent of cracking and increases the peak strength. But at the same time, the ductility of the member is reduced with the increased amount of reinforcement, which is again the typical behaviour of reinforced concrete members [5,66] and can be well captured.

3.5 Summary and current limitations

The proposed model adopted the eigendecomposition procedure to determine the crack planes, where the cyclic normal and shear stress-strain relationships are prescribed. The multiaxial interactions of the orthogonal crack planes due to the Poisson effect are modelled by transforming the true strain tensor to the equivalent uniaxial strains. For the analysis of non-proportional loading cases, the crack plane's shear slip and re-contact behaviour are rigorously modelled, which allows the non-coincidence of the principal stress and principal strain directions. Furthermore, since the constitutive laws are formulated in terms of total strains and internal variables, the numerical implementation of the model has very high robustness.

High confining stress can enhance the strengths and ultimate strains and also change the crack angle under compression. Hence, the assumed crack plane direction defined by Eq. (5) may not be valid for high-confinement cases. The determination of crack plane direction under high confinement would require a flow rule [8]. Therefore, in this study, the applications of the proposed model are restricted to

concrete members subject to low-to-moderate confinement. Yet, the proposed model has the flexibility to be extended to high-confinement applications by incorporating the flow rule and the confining stress effects in the constitutive laws.

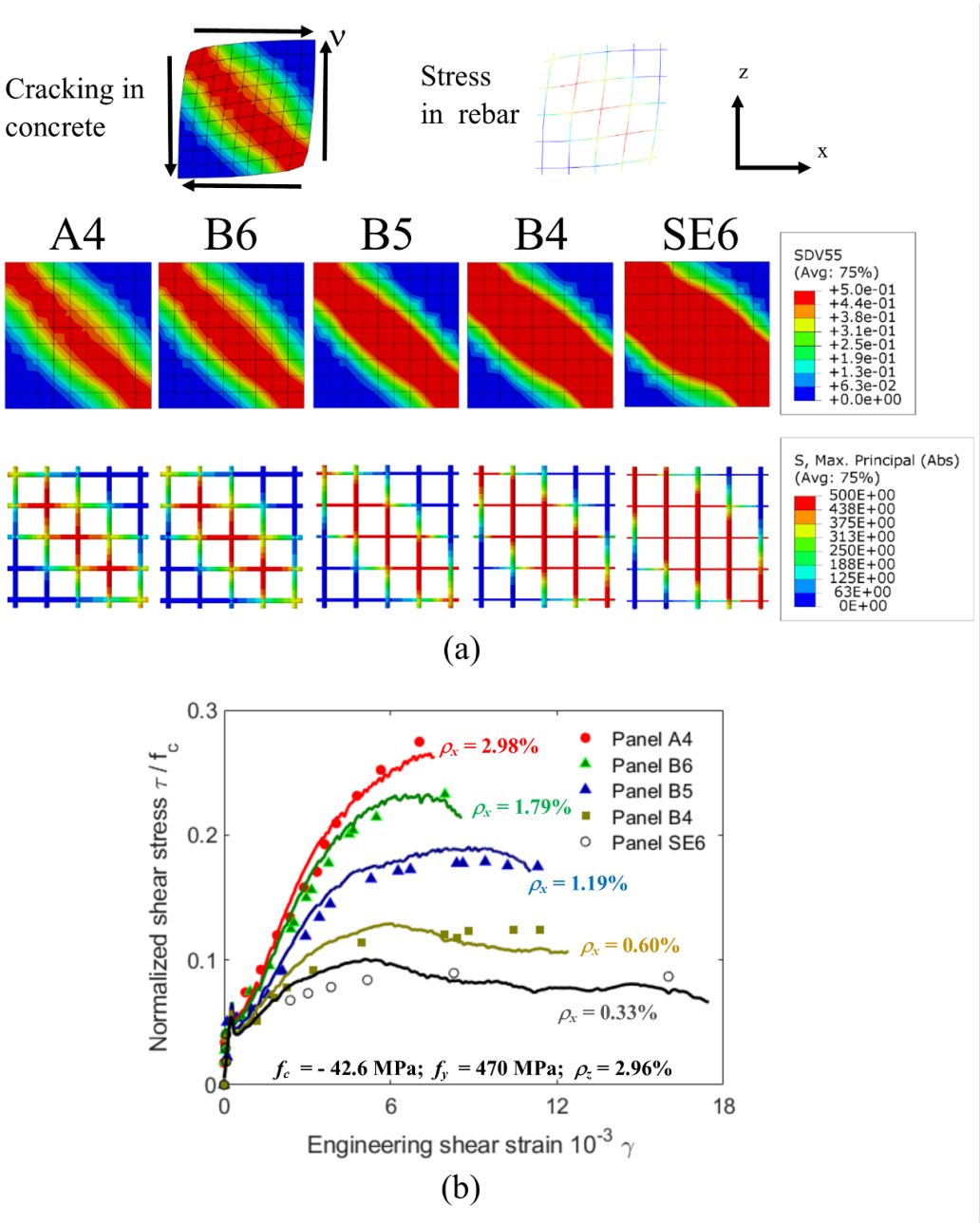

Fig. 12. The panels of various reinforcing ratios are subject to pure shear. (a) The extent of the damage zone and rebar yield zone are more significant in panels with smaller reinforcing ratios. (b) The simulated shear-strain responses (solid lines) agree well with the test data (markers) [28,64,65].

4. Simulation of a full-scale shear-critical RC column test

The previous section has demonstrated that the proposed model could well capture the behaviour of RC elements under typical and non-proportional loading. To further investigate the model performance in simulating the seismic behaviour of concrete structures, a cyclic loading test on a full-scale shear-critical RC column of dimensions = $0.8 \times 0.8 \times 3.2$ m was performed and simulated. The development of NL-FEM of the specimen and the model parameters are presented in section 4.1. The simulated results are presented and compared with the test results in 4.2.

The test was performed using the Multiaxial Testing System (MATS) at the National Centre for Earthquake Engineering Research (NCEER, ROC). The test setup, column dimensions, reinforcement detailing, and the loading protocol are shown in **Fig. 13**. The transverse reinforcement was lightly provided in this column such that it would fail in shear before the yielding of the longitudinal reinforcement. The column was subject to a constant axial load of 2560 kN and varying displacement-controlled horizontal loading. The evolution of the crack patterns of the column during the cyclic loading test is shown in **Fig. 14 (a)**. Although the column was subject to a simple load pattern of a constant vertical load and a cyclic load in the horizontal direction, the local elements would experience non-proportional stress-strain cycles. The formation of inclined shear cracks and the subsequently induced shear stress on the crack planes would interact with the vertical stress and make the principal stress and principal strain coordinates deviate from each other. Furthermore, the low transverse reinforcement ratio also led to low confinement to the core concrete. Hence, this example could best demonstrate the capability of the proposed model without violating the model assumptions.

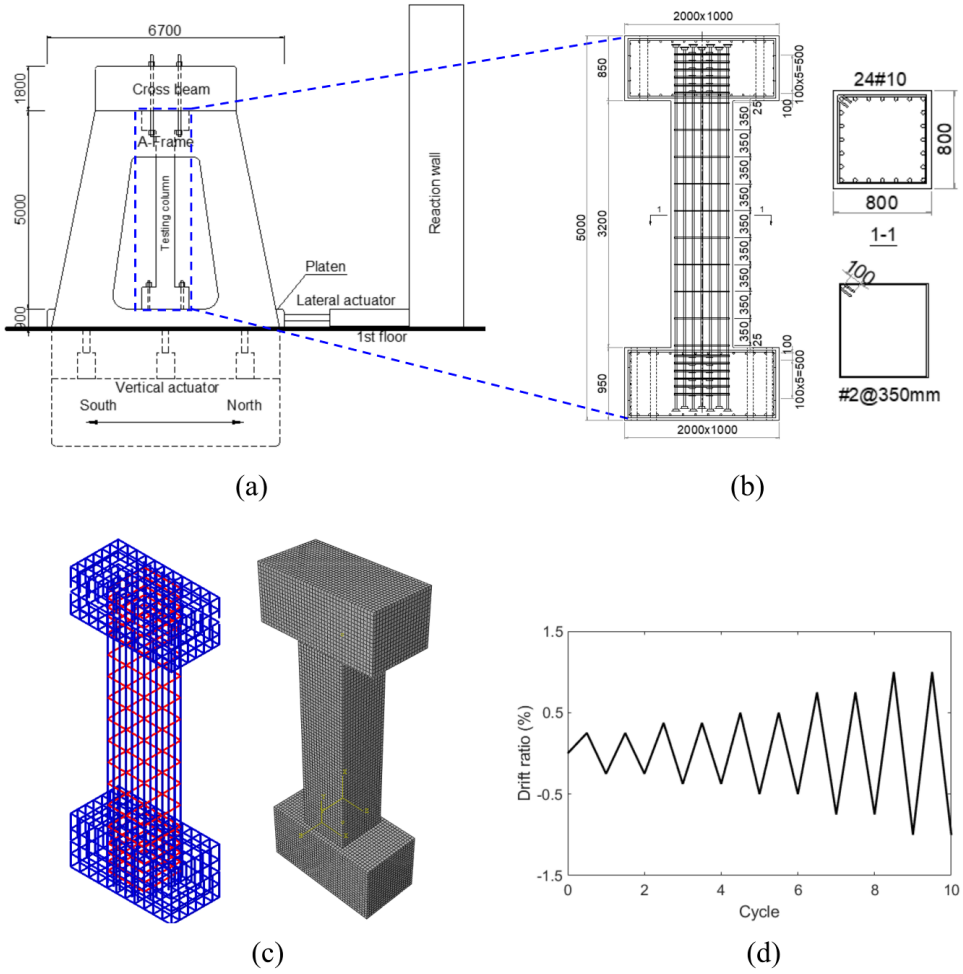

Fig. 13. Full-scale shear-critical RC column test: (a) test set-up; (b) specimen dimensions and reinforcement details; (c) finite element model; (d) loading protocol.

4.1 Finite element modelling

Three-dimensional finite element models, which faithfully reproduce the specimen geometries, were developed using ABAQUS with the material user-subroutine [58] mentioned above. The reinforcing bars were modelled with 2-node linear 3D beam elements, while the concrete was modelled with 8-node linear 3D brick elements. Elastic perfectly plastic stress-strain relationships were applied on the rebar elements. The Young's modulus was 200 GPa, and the tested yield strengths were 473 MPa and 400 MPa for #10 longitudinal rebar and #2 transverse rebar respectively. The compressive strength of concrete was 43MPa. The mesh sensitivity was also investigated, and the tested mesh sizes of both

concrete and rebar elements were 150 mm, 100 mm, and 50 mm. The mesh size-independent and dependent model parameters are summarised in **Table 2**. Meanwhile, the maximum element characteristic lengths for snap-back prevention calculated by Eq. (45) is $\min(l_{ft},\ l_{fc},\ L_{cs}) = \min(254,\ 1827, 1182)$ mm = 254 mm and hence, the selected element sizes do not exceed the limit.

Besides using the proposed concrete model, one simulation was performed using the built-in isotropic hardening continuum damage-plasticity (CDP) model in ABAQUS with 50 mm mesh, which is a modified version of the well-known Barcelona model [7,67]. The CDP requires the input of the monotonic compressive and tensile stress-strain curves to define the hardening or softening of the yield surface. The flow rule is non-associated and is determined by the extended Drucker-Prager surface.

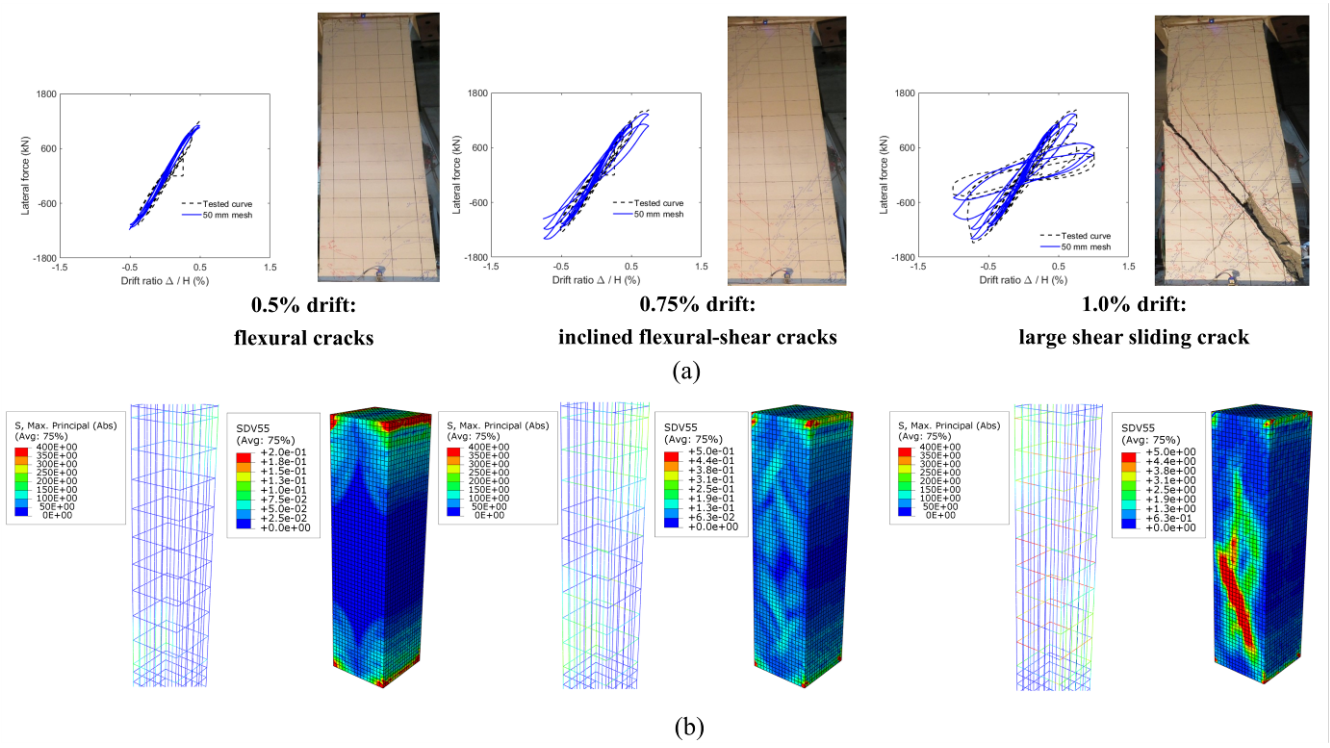

Fig. 14. Comparisons of the tested and simulated column behavior: (a) crack pattern evolution of the tested full-scale shear-critical RC column; (b) the maximum principal stress distribution (σ_{max}) in the rebar and the contour of the equivalent crack width (w_{cr}) in the concrete column.

Table 2. Key model parameters for different mesh sizes

Model parameters	150 mm Mesh	100 mm Mesh	50 mm mesh
E_c (GPa)		22.71	
ν_c		0.2	
f_c (MPa)		-41	
f_r (MPa)		3.57	
b_C		0.5	
ψ		0	
D_a (mm)		20	
β_v		0.2	
μ		0.7	
$\nu_{cr,max}$		1.0	
l_e (mm)	150	100	50
a_c	5.19	7.48	14.33
a_t	1.59	1.39	1.20

For comparing the performances of CDP with the proposed model, the same monotonic (envelope) compressive and tensile stress-strain curves were used. The damage variable evolutions for CDP, which control the unloading behaviour, can be defined by assuming the ratio between the plastic strain ε_p and damage stain ε_d or total inelastic strain ε_{in} [10] as used in the proposed model. If the compressive plastic strain is $\varepsilon_{pc} = b_c\varepsilon_{in,c}$ and $\varepsilon_{dc} = (1 - b_c)\varepsilon_{in}$, then the damage variable can be calculated as

$$d_c = 1 - E_{ec}/E_{ci} = 1 - \sigma_c/\left[(1 - b_c)\varepsilon_{in,c}E_{ci}\right] \quad (46)$$

where $E_{ec} = \sigma_c/\varepsilon_{dc}$ is the effective stiffness. Conventional values were assumed for other parameters used to define the CDP model: the dilation angle = 10^o, flow surface's eccentricity = 0.1, biaxial-to-uniaxial compressive strength ratio = 1.16, and yield surface's shape parameter K = 2/3. The embedded constraint is used to model the interaction between the rebar and concrete elements.

4.2 Results and discussion

The simulated hysteretic loops of applied load against the normalised column drift were shown in **Fig. 15** and compared with the tested curve. **Fig. 16** shows the simulated damage distributions and the plastic strain of the rebar in the columns. The simulated damage pattern and the maximum principal stress distribution in the rebar of the simulation using the proposed model with 50 mm mesh are compared with the test results in **Fig. 14 (b)**. The maximum equivalent crack width in each integration point is stored as a solution-dependent variable in the material subroutine and is defined as

$$w_{cr} = \max_{i=1,2,3} (\varepsilon_{ii} - \varepsilon_{cr}) l_e \geq 0 \tag{47}$$

The flexural cracks formed in the early loading stage of drift = 0.5%, which is consistent with the test observation. Both CPD and the proposed models can capture this behaviour. At increased loading, inclined interacting flexural-shear cracks began to occur at around 0.75% drift (**Fig. 14**), leading to reduced lateral stiffness. Eventually, a large diagonal shear crack occurred when the column was loaded beyond 0.75% to 1.0% drift, where the peak strength was reached, and significant strength degradation occurred afterwards. The yielding of the transverse reinforcement as shown in **Figs. 14(b) & 16(c)** dictated the peak column strength.

Although both CPD and the proposed models could capture the peak strengths and the localised shear damage, the two models exhibited quite different post-peak hysteretic behaviour, as shown in **Fig. 15**. While the CPD model showed a more gradual strength degradation and could not simulate the shear slip behaviour, the proposed model can well capture the degradation and shear slip and re-contact behaviour. This critical difference may arise because the CPD model assumes isotropic hardening/softening rules. The shear stress can be induced on crack planes, and the force transfer mechanisms can vary under non-proportional loading cases, which isotropic models cannot capture. On the other hand, the proposed

model can depict the crack-induced anisotropic responses and multiple force transfer mechanisms of the crack planes, including the shear-slip and re-contact.

Furthermore, as demonstrated in **Figs. 15** and **16**, similar damage patterns and hysteretic behaviour can be obtained in all models with 50 mm, 100 mm, and 150 mm mesh. The sensitivity of the simulations with the proposed model to the mesh size is low. Furthermore, in both experiments and the proposed model simulation, axial damage with vertical propagating cracks in the column was observed in Fig. 14. The loss of axial-load carrying capacity and the vertical cracking of the column is due to the significant shear damage. In summary, the proposed model could well capture the responses of RC members subject to cyclic and non-proportional loading, and the mesh-size sensitivity issue could be significantly reduced.

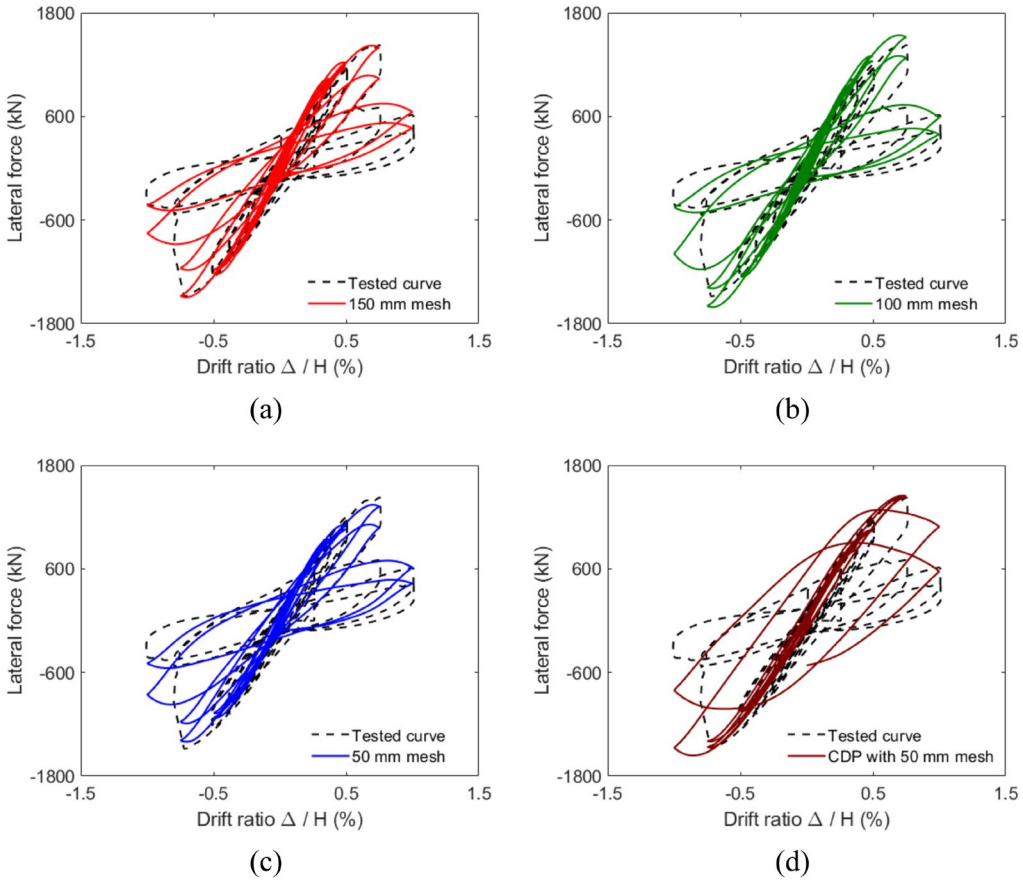

Fig. 15. Simulated and tested hysteretic loops: (a)-(c) proposed model with 150 mm, 100mm, and 50 mm mesh respectively; (b) CDP model with 50 mm mesh.

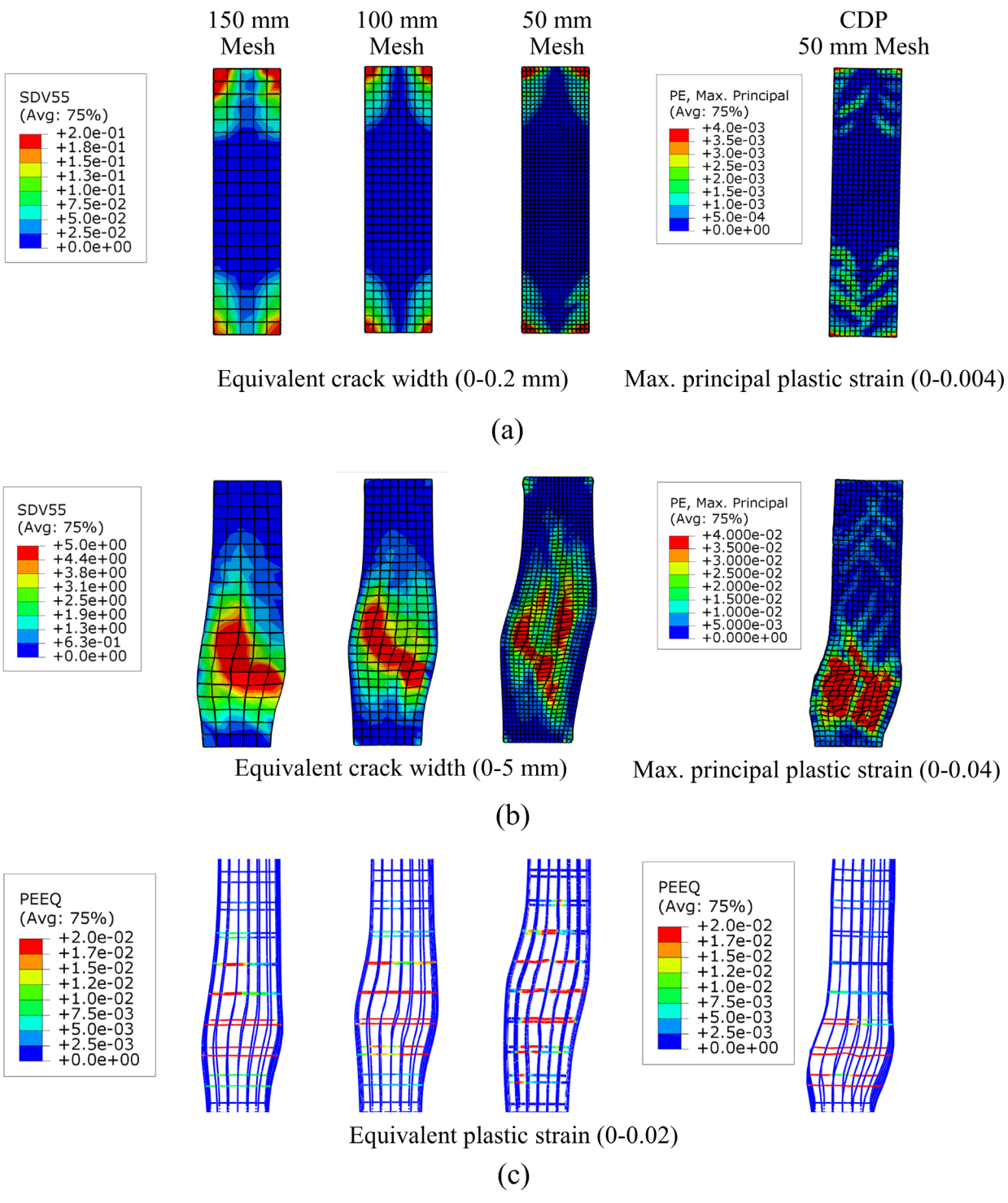

Fig. 16. Comparisons of simulated damage patterns by the proposed model with different mesh sizes and the continuum damage plasticity (CDP) model with 50 mm mesh: (a) damage at drift = 0.5%; (b) damage at drift = 1.0%; (c) plastic strain in rebar at drift = 1.0% (deformation exaggerated 10 times and the states are recorded at the 2nd cycle of each drift level)

Table 3 summarised the energy dissipation, the peak forces, and the residual forces at ±1.0% drift for the numerical simulations and experiment. The simulations with the proposed model generally underestimated the dissipation by about 20%, but the peak forces and residual forces at ±1.0% drift could be captured. On the contrary, although the dissipation for the CDP model was close to the experimental result, the model predicted essentially different hysteretic behaviour and significantly overestimated the residual forces by as much as 85.1%. Moreover, the proposed model with the three mesh sizes could obtain similar forces at different drifts and dissipation. This result demonstrates that the proposed model can effectively mitigate the mesh sensitivity of the global responses.

To further demonstrate the importance of adopting mesh-size dependent model parameters, three load-deflection response simulations were performed again on the column model with 50 mesh size but with three different sets of model parameters, which are calibrated for the characteristic lengths l_e of 50, 100, and 150 mm respectively. The simulated lateral load response histories of the three models are shown in **Fig. 17**. When the columns still exhibit deformation-hardening responses before the peak, the responses are mesh size independent. However, the post-peak softening responses are strongly dependent on the model parameters. The model calibrated for $l_e = 150$ mm exhibits the most severe strength-degradation. As revealed by the energy analysis in Section 3.3, the dissipation at an element with a longer characteristic length is increased under a given strain in the softening region. When the softening responses occur, the deformation is localised. As a result, the strength degradation increases with the increased dissipation in the model with parameters calibrated for a larger l_e.

Furthermore, the analysis time (CPU time), running on Inter® i9-9900KF@3.60 GHz with 4 cores parallelisation, of the proposed model with different mesh sizes and the continuum damage plasticity (CDP) model with 50 mm mesh is compared in **Fig. 18**. The analysis time for the simulations using the proposed model increases nearly exponentially as the mesh size reduces from 150 mm to 50 mm. The analysis time of the 100 mm mesh is about double that of the 150 mm mesh. Although similar global

load-deflection behaviour could be obtained by the proposed models with different mesh sizes, finer mesh sizes could better depict the local responses and damage. Hence, considering the balance of analysis time and details of the local responses, the 100 mm mesh would have the best performance among the three considered mesh sizes. Furthermore, the analysis time of the CDP model with 50 mm mesh is about 1.15 times higher than that of the proposed model with 50 mm mesh.

Table 3. Comparisons of the simulated and experimental responses

	Test	150 mm Mesh	100 mm Mesh	50 mm mesh	CDP 50 mm mesh
Dissipation (MN·m)	27.0	20.9 (-22.6%)[#]	21.5 (-20.4%)	21.8 (-19.3%)	28.2 (+4.4%)
Peak force at + drift (kN)	1429	1420 (-0.6%)	1506 (5.4%)	1368 (4.3%)	1417 (-0.84%)
Peak force at - drift (kN)	-1485	-1495 (0.7%)	-1595 (7.4%)	-1396 (-6.0%)	-1551 (4.4%)
Force at +1.0% drift (kN)[^]	409	463.8 (13.4%)	405.7 (-0.8%)	430 (5.1%)	569.6 (39.3%)
Force at -1.0% drift (kN)	-435	-431.1 (-0.9%)	-467.4 (7.4%)	-485 (11.5%)	-805 (85.1%)

[^]The force recorded at the second drift cycle; [#] percentage difference compared to the test result.

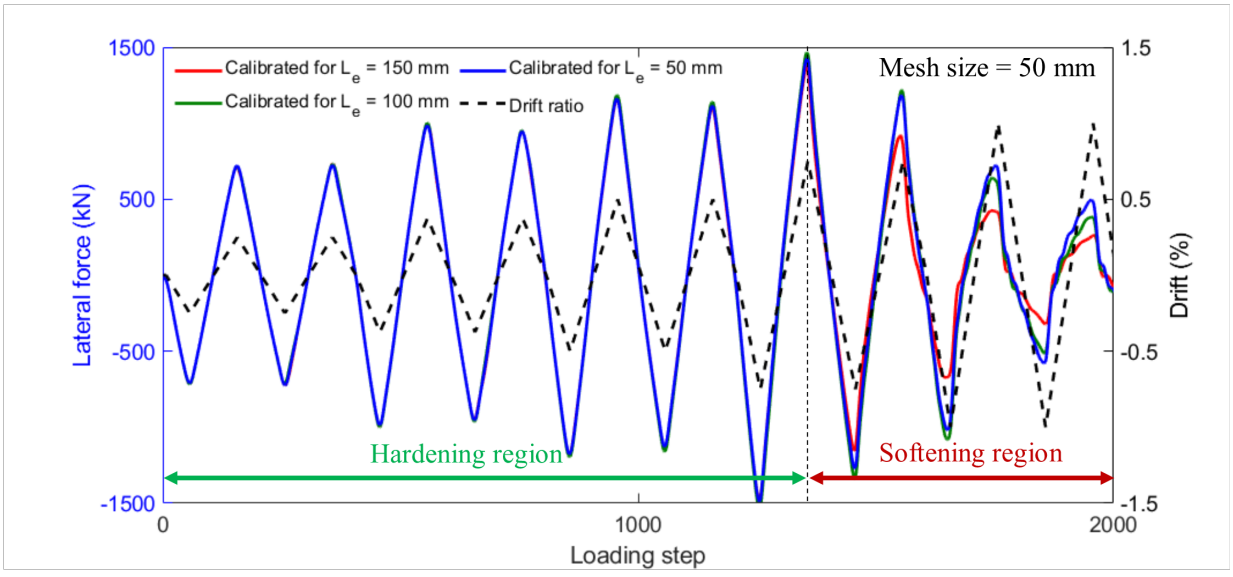

Fig. 17. Evolutions of the simulated lateral load on the column with the same mesh size (50 mm) but different model parameters calibrated for varying l_e.

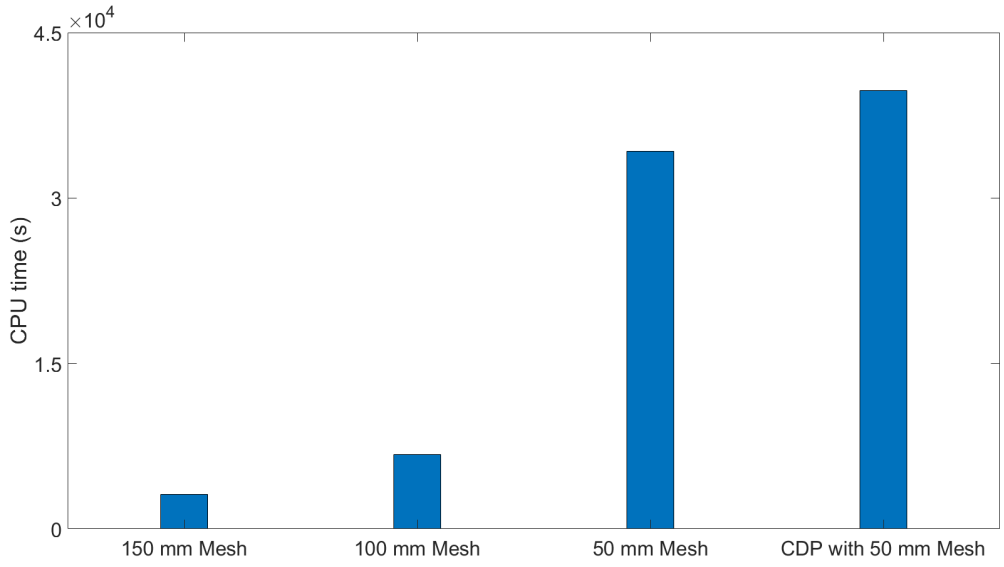

Fig. 18. Comparisons of analysis time by the proposed model with different mesh sizes and the continuum damage plasticity (CDP) model with 50 mm mesh.

5. Conclusions

The modern and emerging generation of concrete structures are featured with irregular shapes. Their analysis and design for safety under extreme loading, including earthquakes and hurricanes, have imposed challenges to structural designers. The nonlinear behaviour of such structures is well beyond the limitations of prevailing design standards, and conventional constitutive models may not adequately model their behaviour. Given this, this paper presents a novel, robust, mesh-sensitivity reduced, efficient, and rigorously formulated-constitutive model for simulating the nonlinear three-dimensional responses of concrete structures under non-proportional and cycle loading.

In the proposed model, the crack planes are uniquely searched and fixed using the eigendecomposition method and a novel local crack plane searching algorithm. The mechanical responses of the crack planes are rigorously depicted by the proposed cyclic axial stress-strain and modified shear retention models.

Furthermore, the mesh sensitivity issue due to the material softening was mitigated by regularising the mesh-size dependent model parameters. The model was implemented into ABAQUS's user subroutine. The proposed model can reasonably simulate a wide range of nonlinear and cyclic behaviour of plain concrete and reinforced concrete elements under regular or non-proportional loading.

A cyclic loading test on a full-scale shear-critical RC column was performed and simulated to validate the applicability of the proposed model. The simulations can successfully capture the early flexural cracking, localised shear cracking in the late loading stage and the complete load-deflection hysteresis responses. While the proposed model can adequately capture the anisotropic, crack-slip, and re-contact responses, the isotropic-hardening continuum damage plasticity model would encounter difficulties in simulating the crack-slip responses.

Acknowledgement

The authors would like to express their gratitude for the funding support by the Ministry of Science and Technology (MOST), R.O.C. under Grand Numbers 110-2221-E-A49 -133 -, 109-2636-E-006-015, 109-2636-E-009 -015-., and Royal Academy of Engineering-Industrial Fellowship (IF\192023).

Reference

[1] C.R.Gagg, Cement and concrete as an engineering material: An historic appraisal and case study analysis, Eng. Fail. Anal. 40 (2014) 114–140. https://doi.org/10.1016/j.engfailanal.2014.02.004.

[2] American Concrete Institute, Building code requirements for structural concrete (ACI 318–19) and Commentary, Farmington Hills, MI: ACI, 2019.

[3] CEN, Eurocode 2: design of concrete structures. Part 1: general rules and rules for buildings (EN 1992–1-1:2004), European Committee for Standardization, Brussels, 2004.

[4] J.Zhang, J.Wang, S.Dong, X.Yu, B.Han, A review of the current progress and application of 3D printed concrete, Compos. Part A Appl. Sci. Manuf. 125 (2019) 105533. https://doi.org/10.1016/j.compositesa.2019.105533.

[5] J.Moehle, Seismic Design of Reinforced Concrete Buildings, McGraw-Hill, New York., 2015.

[6] M.N.Fardis, E.C.Carvalho, P.Fajfar, A.Pecker, Seismic Design of Concrete Buildings to Eurocode 8, CRC Press, 2015.

[7] J.Lubliner, J.Oliver, S.Oller, E.Oñate, A plastic-damage model for concrete, Int. J. Solids Struct. 25 (1989) 299–326. https://doi.org/10.1016/0020-7683(89)90050-4.

[8] W.F.Chen, Plasticity in Reinforced Concrete, McGraw-Hill, New York., 1982.

[9] K.T.Wan, H.Zhu, T.Y.P.Yuen, B.Chen, C.Hu, C.K.Y.Leung, J.S.Kuang, Development of low drying shrinkage foamed concrete and hygro-mechanical finite element model for prefabricated building fasçade applications, Constr. Build. Mater. 165 (2018) 939–957. https://doi.org/10.1016/j.conbuildmat.2018.01.024.

[10] W.B.Krätzig, R.Pölling, An elasto-plastic damage model for reinforced concrete with minimum number of material parameters, Comput. Struct. 82 (2004) 1201–1215. https://doi.org/10.1016/j.compstruc.2004.03.002.

[11] T.Dede, Y.Ayvaz, Comparative study of plasticity models for concrete material by using different criteria including Hsieh–Ting–Chen criterion, Mater. Des. 31 (2010) 1482–1489. https://doi.org/10.1016/j.matdes.2009.08.026.

[12] M.Li, Y.Deng, H.Zhang, S.H.F.Wong, A.Mohamed, Y.Zheng, J.Gao, T.Y.P.Yuen, B.Dong, J.S.Kuang, Topology optimization of multi-material structures with elastoplastic strain hardening model, Struct. Multidiscip. Optim. (2021). https://doi.org/10.1007/s00158-021-02905-3.

[13] R.Desmorat, Anisotropic damage modeling of concrete materials, Int. J. Damage Mech. 25 (2016) 818–852. https://doi.org/10.1177/1056789515606509.

[14] G.Z.Voyiadjis, Z.N.Taqieddin, P.I.Kattan, Anisotropic damage–plasticity model for concrete, Int. J. Plast. 24 (2008) 1946–1965. https://doi.org/10.1016/j.ijplas.2008.04.002.

[15] Y.P.Yuen, J.S.Kuang, Fourier-based incremental homogenisation of coupled unilateral damage–plasticity model for masonry structures, Int. J. Solids Struct. 50 (2013) 3361–3374. https://doi.org/10.1016/j.ijsolstr.2013.06.001.

[16] J.Lemaitre, R.Desmorat, Engineering Damage Mechanics - Ductile, Creep, Fatigue and Brittle Failures, Springer-Verlag Berlin Heidelberg, 2005.

[17] T.Y.P.Yuen, T.Deb, H.Zhang, Y.Liu, A fracture energy based damage-plasticity interfacial constitutive law for discrete finite element modelling of masonry structures, Comput. Struct. 220 (2019) 92–113. https://doi.org/10.1016/j.compstruc.2019.05.007.

[18] M.A.Wardeh, H.A.Toutanji, Parameter estimation of an anisotropic damage model for concrete using genetic algorithms, Int. J. Damage Mech. 26 (2017) 801–825. https://doi.org/10.1177/1056789515622803.

[19] Z.P.Bažant, P.C.Prat, Microplane Model for Brittle-Plastic Material: I. Theory, J. Eng. Mech. 114 (1988) 1672–1688. https://doi.org/10.1061/(ASCE)0733-9399(1988)114:10(1672).

[20] I.Carol, Z.P.Bazant, Damage and plasticity in microplane theory, Int. J. Solids Struct. 34 (1997) 3807–3835. https://doi.org/10.1016/S0020-7683(96)00238-7.

[21] J.Ožbolt, Y.Li, I.Kožar, Microplane model for concrete with relaxed kinematic constraint, Int. J. Solids Struct. 38 (2001) 2683–2711. https://doi.org/10.1016/S0020-7683(00)00177-3.

[22] P.Bažant, B.H.Oh, Efficient Numerical Integration on the Surface of a Sphere, ZAMM - J. Appl. Math. Mech. / Zeitschrift Für Angew. Math. Und Mech. 66 (1986) 37–49. https://doi.org/10.1002/zamm.19860660108.

[23] F.C.Caner, Z.P.Bažant, Microplane Model M7 for Plain Concrete. II: Calibration and Verification, J. Eng. Mech. 139 (2013) 1724–1735. https://doi.org/10.1061/(ASCE)EM.1943-7889.0000571.

[24] K.Kirane, M.Salviato, Z.P.Bažant, Microplane triad model for simple and accurate prediction of orthotropic elastic constants of woven fabric composites, J. Compos. Mater. 50 (2016) 1247–1260. https://doi.org/10.1177/0021998315590264.

[25] V.Travaš, J.Ožbolt, I.Kožar, Failure of plain concrete beam at impact load: 3D finite element analysis, Int. J. Fract. 160 (2009) 31–41. https://doi.org/10.1007/s10704-009-9400-1.

[26] G.DiLuzio, A symmetric over-nonlocal microplane model M4 for fracture in concrete, Int. J. Solids Struct. 44 (2007) 4418–4441. https://doi.org/10.1016/j.ijsolstr.2006.11.030.

[27] F.J.Vecchio, M.P.Collins, The Modified Compression-Field Theory for Reinforced Concrete Elements Subjected to Shear, ACI J. 19 (1986) 219–223.

[28] E.C.Bentz, F.J.Vecchio, M.P.Collins, Simplified modified compression field theory for calculating shear strength of reinforced concrete elements, ACI Struct. J. 103 (2006) 614–624.

[29] X.-B.D.Pang, T.T.C.Hsu, Fixed angle softened truss model for reinforced concrete, ACI Struct. J. 93 (1996) 196–208.

[30] T.T.Hsu, R.H.Zhu, Softened Membrane Model for Reinforced Concrete Elements in Shear, ACI Struct. J. 99 (2002) 460–469. https://doi.org/10.14359/12115.

[31] M.S.Barkhordari, M.Tehranizadeh, M.H.Scott, Numerical modelling strategy for predicting the response of reinforced concrete walls using Timoshenko theory, Mag. Concr. Res. (2021) 1–23. https://doi.org/10.1680/jmacr.19.00542.

[32] C.H.Luu, Y.L.Mo, T.T.C.Hsu, Development of CSMM-based shell element for reinforced concrete structures, Eng. Struct. 132 (2017) 778–790. https://doi.org/10.1016/j.engstruct.2016.11.064.

[33] A.Laskar, Y.L.Mo, T.T.C.Hsu, Simulation of post-tensioned bridge columns under reversed-cyclic loads, Mater. Struct. 49 (2016) 2237–2256. https://doi.org/10.1617/s11527-015-0646-y.

[34] T.G.Mondal, S.S.Prakash, Improved softened truss model for RC circular columns under combined torsion and axial compression, Mag. Concr. Res. 67 (2015) 855–866. https://doi.org/10.1680/macr.14.00087.

[35] K.Maekawa, H.Okamura, A.Pimanmas, Nonlinear Mechanics of Reinforced Concrete, 1st ed., CRC Press, 2003.

[36] K.Orakcal, L.M.Massone, D.Ulugtekin, A Hysteretic Constitutive Model for Reinforced Concrete Panel Elements, Int. J. Concr. Struct. Mater. 13 (2019) 51. https://doi.org/10.1186/s40069-019-0365-9.

[37] C.-C.Hung, S.-H.Li, Three-dimensional model for analysis of high performance fiber reinforced cement-based composites, Compos. Part B Eng. 45 (2013) 1441–1447. https://doi.org/10.1016/j.compositesb.2012.08.004.

[38] T.R.S.Mullapudi, A.Ayoub, Analysis of Reinforced Concrete Columns Subjected to Combined Axial, Flexure, Shear, and Torsional Loads, J. Struct. Eng. 139 (2013) 561–573. https://doi.org/10.1061/(ASCE)ST.1943-541X.0000680.

[39] C.Liu, Y.Yang, J.-J.Wang, J.-S.Fan, M.-X.Tao, Y.L.Mo, Biaxial reinforced concrete constitutive models for implicit and explicit solvers with reduced mesh sensitivity, Eng. Struct. 219 (2020) 110880. https://doi.org/10.1016/j.engstruct.2020.110880.

[40] T.Deb, T.Y.P.Yuen, D.Lee, R.Halder, Y.You, Bi-directional collapse fragility assessment by DFEM of unreinforced masonry buildings with openings and different confinement configurations, Earthq. Eng. Struct. Dyn. (2021). https://doi.org/10.1002/eqe.3547.

[41] M.Á.Caminero, F.J.Montáns, K.-J.Bathe, Modeling large strain anisotropic elasto-plasticity with logarithmic strain and stress measures, Comput. Struct. 89 (2011) 826–843. https://doi.org/10.1016/j.compstruc.2011.02.011.

[42] W.-F.Chen, Plasticity in Reinforced Concrete, J. Ross Publishing, 2007.

[43] J.G.M.vanMier, Concrete Fracture: A Multiscale Approach, Taylor & Francis Group, New York, 2013.

[44] V.C.Li, A simplified micromechanical model of compressive strength of fiber-reinforced cementitious composites, Cem. Concr. Compos. 14 (1992) 131–141. https://doi.org/10.1016/0958-9465(92)90006-H.

[45] H.Horii, S.Nemat-Nasser, Brittle failure in compression: splitting faulting and brittle-ductile transition, Philos. Trans. R. Soc. London. Ser. A, Math. Phys. Sci. 319 (1986) 337–374. https://doi.org/10.1098/rsta.1986.0101.

[46] ACI Committee 224, Control of Cracking in Concrete Structures, ACI J. Proc. 69 (1972) 717–753.

[47] H.Nakamura, H.Takeshi, Compressive fracture energy and fracture zone length of concrete, in: US-Japan Semin. Post-Peak Behav. Reinf. Concr. Struct. Subj. to Seism. Loads Recent Adv. Challenges Anal. Des., Tokyo, Japan, 2000: pp. 471–487.

[48] M.Mansour, T.T.C.Hsu, Behavior of Reinforced Concrete Elements under Cyclic Shear. II: Theoretical Model, J. Struct. Eng. 131 (2005) 54–65. https://doi.org/10.1061/(ASCE)0733-9445(2005)131:1(54).

[49] K.Kolozvari, K.Orakcal, J.W.Wallace, Modeling of Cyclic Shear-Flexure Interaction in Reinforced Concrete Structural Walls. I: Theory, J. Struct. Eng. 141 (2015) 04014135. https://doi.org/10.1061/(ASCE)ST.1943-541X.0001059.

[50] S.K.Paul, A critical review of experimental aspects in ratcheting fatigue: microstructure to specimen to component, J. Mater. Res. Technol. 8 (2019) 4894–4914. https://doi.org/10.1016/j.jmrt.2019.06.014.

[51] J.C.Walraven, Fundamental analysis of aggregate interlock, J. Struct. Div. ASCE. 107 (1981) 2245–2270.

[52] H.Salem, K.Maekawa, Spatially averaged tensile mechanics for cracked concrete and reinforcement under highly inelastic range., J. Mater. Concr. Struct. Pavements, JSCE. 42 (1999) 277–293. https://doi.org/10.2208/jscej.1999.613_277.

[53] CEB-FIP, Model Code 2010 - Final version, Vol. 1, fédération internationale du béton, Bulletin 66, Lausanne, Switzerland, 2012. https://doi.org/10.1007/s13398-014-0173-7.2.

[54] C.-C.Hung, Y.-F.Su, K.-H.Yu, Modeling the shear hysteretic response for high performance fiber reinforced cementitious composites, Constr. Build. Mater. 41 (2013) 37–48. https://doi.org/10.1016/j.conbuildmat.2012.12.010.

[55] S.Balakrishnan, D.W.Murray, Concrete constitutive model for NLEE analysis of structures, J. Struct. Eng. 114 (1988) 1449–1466. https://doi.org/10.1061/(ASCE)0733-9445(1988)114:7(1449).

[56] W.Chung, S.H.Ahmad, Analytical model for shear critical reinforced-concrete members, J. Struct. Eng. 121 (1995) 1023–1029. https://doi.org/10.1061/(ASCE)0733-9445(1995)121:6(1023).

[57] C.-H.Jeng, T.T.C.Hsu, A softened membrane model for torsion in reinforced concrete members, Eng. Struct. 31 (2009) 1944–1954. https://doi.org/10.1016/j.engstruct.2009.02.038.

[58] ABAQUS Inc., Abaqus/Explicit User Subroutines: VUMAT, in: Abaqus User Subroutines Ref. Guid., 2020.

[59] CEN Comité Européen de Normalisation, BS EN 1992-1-1:2004+A1:2014 Eurocode 2: Design of concrete structures. General rules and rules for buildings, BSI, London, UK, 2014.

[60] H.Kupfer, H.K.Hilsdorf, H.Rusch, Behavior of concrete under biaxial stresses, ACI Mater. J. 66 (1969) 656–666.

[61] T.H.A.Nguyen, T.Q.Bui, S.Hirose, Smoothing gradient damage model with evolving anisotropic nonlocal interactions tailored to low-order finite elements, Comput. Methods Appl. Mech. Eng. 328 (2018) 498–541. https://doi.org/10.1016/j.cma.2017.09.019.

[62] Z.P.Bažant, B.H.Oh, Crack band theory for fracture of concrete, Matériaux Constr. 16 (1983) 155–177. https://doi.org/10.1007/BF02486267.

[63] C.Rosselló, M.Elices, G.V.Guinea, Fracture of model concrete: 2. Fracture energy and characteristic length, Cem. Concr. Res. 36 (2006) 1345–1353. https://doi.org/10.1016/j.cemconres.2005.04.016.

[64] X.Pang, T.T.C.Hsu, Behavior of reinforced concrete membranes in shear, ACI Struct. J. 92 (1995) 665–679.

[65] U.Kirschner, M.P.Collins, Investigating the Behaviour of Reinforced Concrete Shell Elements, 1986.

[66] T.Paulay, M.J.N.Priestley, Seismic Design of Reinforced Concrete and Masonry Buildings, John Wiley & Sons, Inc., 1992.

[67] J.Lee, G.L.Fenves, A plastic-damage concrete model for earthquake analysis of dams, Earthq. Eng. Struct. Dyn. 27 (1998) 937–956. https://doi.org/10.1002/(SICI)1096-9845(199809)27:9<937::AID-EQE764>3.0.CO;2-5.